Woods Hole Oceanographic Institution

Flow Distortion Investigation of Wind Velocity Perturbations for Two Ocean Meteorological Platforms

by

Marc Emond,[1] Doug Vandemark,[1] James Forsythe,[1] Al Plueddemann,[2] Tom Farrar,[2]

Woods Hole Oceanographic Institution
Woods Hole, MA 02543

March 2012

Technical Report

Upper Ocean Processes Group
Woods Hole Oceanographic Institution
Woods Hole, MA 02543
UOP Technical Report 2012-01

[1] University of New Hampshire
[2] Woods Hole Oceanographic Institution

WHOI-2012-02

Flow Distortion Investigation of Wind Velocity Perturbations for Two Ocean Meteorological Platforms

by

Marc Emond, Doug Vandemark, James Forsythe, Al Plueddemann, Tom Farrar

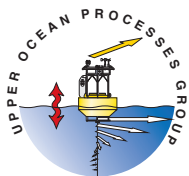Woods Hole Oceanographic Institution
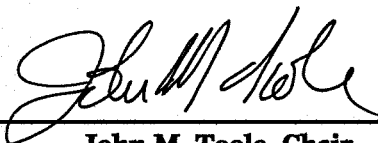Woods Hole, Massachusetts 02543

March 2012

Technical Report

Approved for Distribution:

_____
John M. Toole, Chair
Department of Physical Oceanography

Abstract

A computational fluid dynamics (CFD) study was performed of the wind flow around two ocean buoys used to collect meteorological data from sensors mounted on the buoy tower. The CFD approach allowed wind velocity perturbations to be evaluated as a step towards quantifying the impacts of flow distortion on buoy wind measurements. The two buoys evaluated were the Wood Hole Oceanographic Institution WHOI Modular Ocean Buoy System and the University of New Hampshire (UNH) 2.1 m discus buoy. Engineering drawings were used to create a computational mesh for each buoy. Suitable solution methods were then developed and tested, CFD simulations were performed, and the results evaluated. Eleven CFD runs were performed, six for the WHOI buoy and five for the UNH buoy. Highlights of analysis for the WHOI buoy were that horizontal flow distortion was relatively small (<1%) for head-on flow, but that the tendency of the buoy to establish an angle of about 30 degrees relative to the flow resulted in acceleration at one anemometer location and deceleration at the other. Highlights of the analysis for the UNH buoy were that flow distortion of about 5% at the wind sensor location could be cut by about a factor of two by either raising the sensor by 2 ft or removing solar panels.

Table of Contents

List of Figures

List of Tables

1. Introduction

   This report documents a computational fluid dynamics (CFD) study of the wind flow around two ocean observing buoys used to collect meteorological data using sensors mounted near the top of buoy towers. The two buoys under study are the Wood Hole Oceanographic Institution (WHOI) Modular Ocean Buoy System (MOBS; Colbo and Weller, 2009), a 2.8 m diameter discus-type platform shown in Fig. 1, and the Univ. of New Hampshire (UNH; Irish et al., 2010) 2.1 m discus buoy, first used in the Global Ocean Ecosystem Dynamics (GLOBEC) program. The main study objective is to obtain CFD predictions for anticipated flow distortion in the horizontal and vertical velocity components at the wind measurement locations on top of these buoys. This is partially motivated by observed flow distortions around the UNH platform as well as WHOI interest in quantifying possible platform impacts on the horizontal wind and direct covariance measurements obtained on MOBS using their twin ASIMET and DCFS systems. The study was performed at UNH in summer 2010 and consisted of collecting and/or creating CAD drawings for the two platforms, developing a model mesh for these platforms suitable for input to ANSYS CFD solvers, developing and testing suitable solution methods, and then performing CFD simulations, evaluating the results, and providing a summary assessment to the buoy field measurement and design teams.
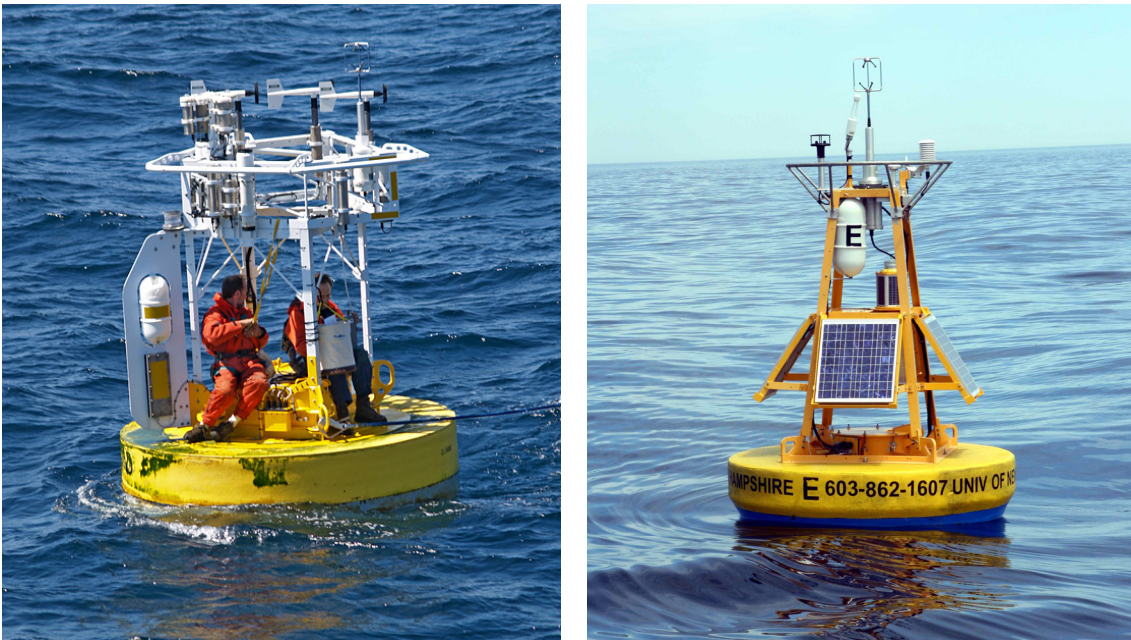

Figure 1. The WHOI MOBS buoy at left and the UNH 2.1 m discus buoy at right.

The report is organized as follows. Section 2 describes the CDF modeling methods. Section 3 presents results from 11 CDF runs, including summary statistics and discussions of each run. Figures referred to in Sec. 3 are presented in the Appendix.

2. Methods

In this investigation, the flow modeling software ANSYS Fluent was used to simulate the airflow around the two buoy models (http://www.ansys.com/Products) ANSYS packages their flow modeling software with its own solid modeling and meshing tools. ANSYS DesignModeler is the integrated modeling tool and ANSYS Mesher is the meshing Utility. DesignModeler was used to edit the buoy models for use by Fluent and Mesher. The UNH model was drawn from scratch using the modeler while the WHOI model was imported from an external CAD program (SolidWorks).

The UNH and WHOI buoy models were both simplified from their full drawings to save on computing time as well as to better integrate with the Mesher. Many of the smaller parts, especially those far from the points of interest and thought to have little influence on the flow, were taken out of the models. These included nuts, bolts, small diagonal braces, gussets, and some small curvatures. While these parts have little effect on the flow, their small size requires a highly refined mesh to resolve their shapes. The time and spatial scale of the resulting flow distortion caused by these parts are small enough to be neglected, while their removal significantly improves the efficiency of the calculations.

One specific simplification of interest, on the WHOI model, was the removal of a large number of drilled holes in the angle iron constituting the buoy super structure. The prevalence of these holes at first caused some doubt as to whether they could be removed without affecting the overall flow. A test simulation was run on a simplified model of an angle iron piece with and without holes to compare the resulting downstream flow characteristics (using realistic Re Numbers). Figure A1 illustrates the flow characteristics past both test pieces. This is a top view of the two angle-iron pieces with the drilled version on the bottom and the mean flow to the right. The horizontal velocity vector (in the mean stream direction) is contoured at a horizontal plane through one of the drilled holes. The disturbance caused by the non-drilled piece (top) is clearly slightly larger than the drilled version. However, looking at the downstream velocity directly behind each piece at just 1 ft away shows that the flows are very similar - the difference between the observed velocities is only 0.11% with respect to the inflow velocity. At 2 ft this difference drops further to 0.04%, and so on. These differences were small enough that it was determined that the effect of removing the holes was negligible and worth the effort to save on computation time.

Once simplified, the solid models were subtracted from a fluid body, leaving a buoy shaped void. The resulting body is the model of the fluid surrounding the buoy. These models consist of a rectangular box with the buoy void centered and sitting at the bottom. The bottom represents the waterline as the lower boundary of the air flow. The top and side outer boundaries are defined far enough away from the buoy to avoid their affecting the flow near the center. During the simulations, air enters one side of the box, passes the buoy, and exits the opposite side, as in a wind tunnel. Specifics of the model boundary conditions are discussed below.

This process of creating a fluid model by subtracting the solid models created some complications. First off, this required the solid model to be "air tight", meaning that there were no open faces for the fluid to flow into the solid structure. A simple example would be a surface

model of a solid cube. If two of the faces were not connected properly or if there were a hole in one face, the fluid would be allowed to "flow" into the inside of the box. In modeling, if the solid model of the box were subtracted from a fluid body the resulting body would include the fluid inside the box connected to the outside by the small space or hole. Another example is a model of a bolt that is supposed to fit tightly into a hole. If the bolt is slightly misaligned leaving a space between it and the hole, once subtracted this will leave a very small crescent shaped fluid body. Although this type of small fluid body is unimportant for the flow simulation, it will take a highly refined mesh to resolve and will take computational power away from the more pertinent flow computations. These types of problems proved difficult to locate and correct in the complex WHOI CAD model.

Another fluid modeling complication was the formation of non-manifold bodies. Specifically, in DesignModeler, a non-manifold body is any body that contains an edge connecting more than two faces. Many of these bodies showed up during the original attempts to subtract the solid model from the fluid body. This issue took many small yet time consuming CAD edits to rectify.

Once the problem areas were identified and taken out, and the associated simplifications completed, the fluid model was meshed using the ANSYS meshing utility. A non-viscous tetrahedral mesh method was used because of the high geometric complexity of the models. The tetrahedral meshing method is able to fill any arbitrary space automatically and quickly. This was essential given the project time constraints and the variability in the shapes involved. Choosing a non-viscous grid meant neglecting to resolve the viscous boundary layers at the structure's surfaces. Not doing so would have meant refining the mesh along each surface and slowly inflating the cells normally throughout the boundary layer region. We assume this would have added undue time and complexity to the meshing process as well as a drastically longer simulation run time due to the added number of cells. Because the main purpose of the simulations in this case was to look at major blockage effects at the sensor locations, an accurate representation of viscous drag was not required. Many of the larger bodies on the buoys have sharp edges; the boundary layer separation on these can be predicted adequately without a viscous grid. However, the bodies with more rounded shapes, including some of the sensors, will show earlier boundary layer separation which is not properly indicative of the flow.

In order to evaluate the influence of viscous flow, a comparative test was completed with a sample cylindrical body with a Reynolds number in the range of that seen in the models. The simulation compared the flow around the body with and without a viscous grid. Figures V-1 and V-2 illustrate the results of the viscous and non-viscous runs, respectively. The output from the viscous run looked approximately like the theoretical flow while the non-viscous run showed a later separation point and in turn a tighter wake. The flow close to the cylinder is therefore much different between the two, as is evident in the figures. A test to determine the effect this difference has at the buoy sensors considered the cylinder as the crash bar on the WHOI buoy. The relative position of the vane anemometer was then examined to look at the velocity percentage differences between the two runs. These differences are 1.27% and 0.424%, respectively for horizontal and vertical velocities. It was assumed that these small differences would be overshadowed by the larger flow distortions. Because of this simplification though, the

results should be considered to be indicative rather than definitive, future studies should evaluate results that include viscous effects for surfaces with relatively large cross section.

The final mesh for each model instance was chosen through an iterative process based on the number of cells and the associated run time in Fluent. Adjusting the mesh involved setting the cell minimum and maximum size/face size as well as the growth rate. The minimum cell size was scoped to resolve the smallest geometric features while the max size was kept at a minimum but limited by the number of cells. As the number of cells approached 10e6 the meshing utility began to tax the quad core processor physical memory (16 G). In the end the meshes for the WHOI models averaged 7-8 million cells and the UNH models averaged 4-5 million. The final time to mesh averaged between 25 minutes and 2 hours. Figures 2 and 3 illustrate the Full WHOI Model mesh and Figure 4 shows the UNH buoy mesh.

Once meshed, the models were loaded into Fluent. Fluent was run in double precision solver mode for overall higher accuracy. This was especially important in areas of high cell aspect ratios and those with a high contrast in length scales. Parallel processing was used to speed up the run time. The four processes were split between the four processors on the quad core. The model mesh for each run is partitioned by the software. Each processor handles one partition and its particular data set. The processes are synchronized with commands and data passed between them by a central compute node. This parallel processing feature drastically reduced the simulation run times. This was important since some runs took as long as three days - more on run times below.
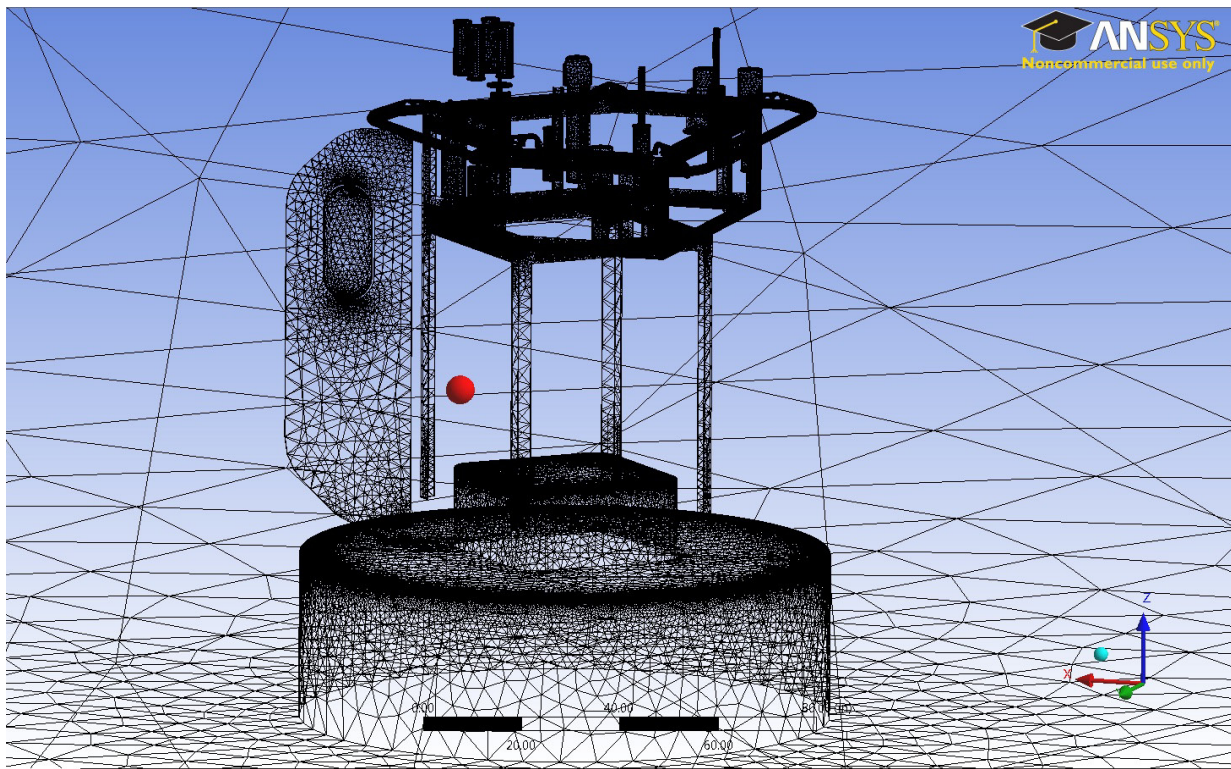

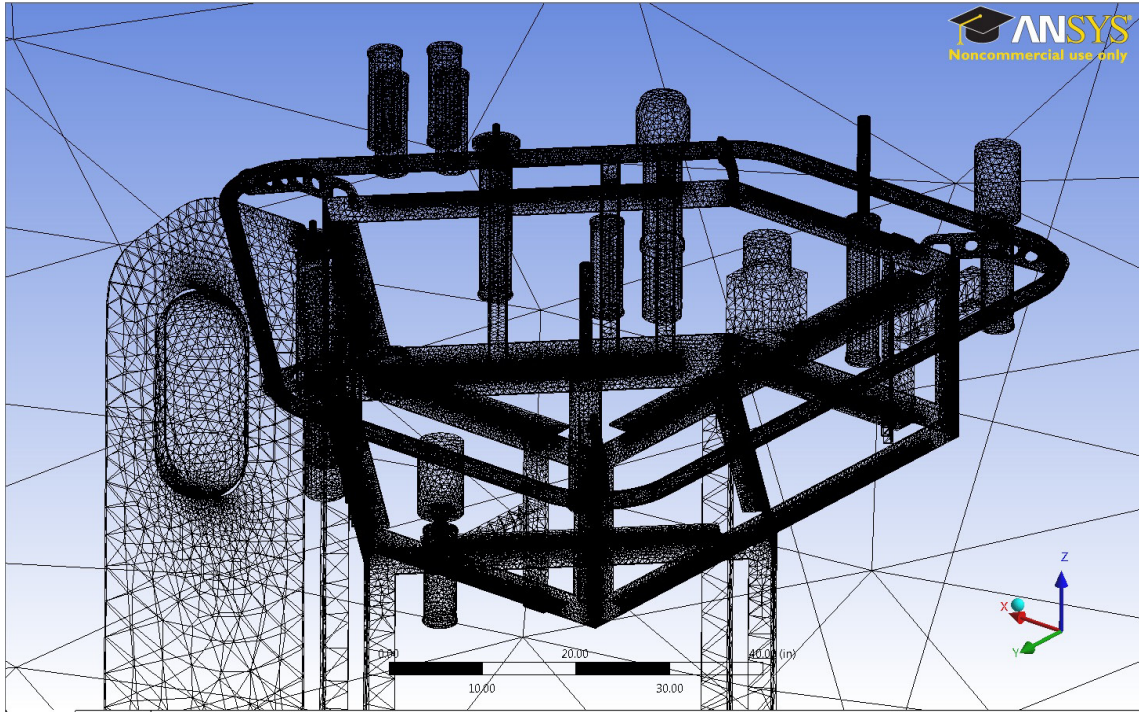**Figure 2.** CFD mesh for full WHOI MOBS, View 1.

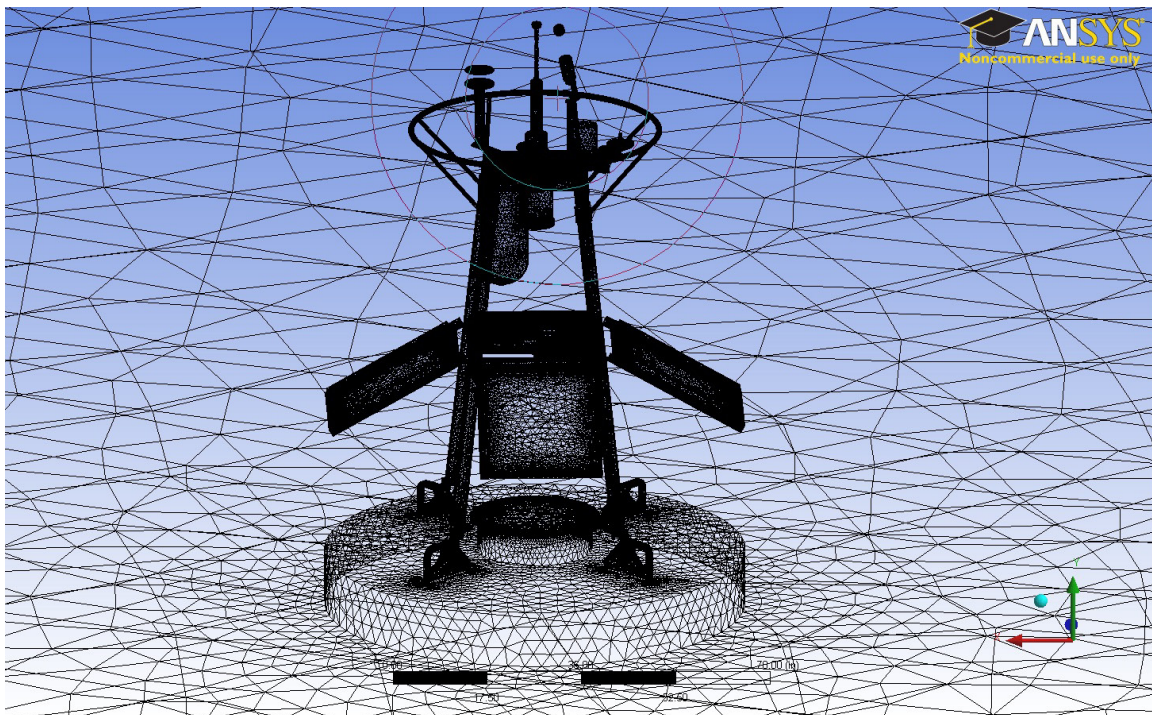**Figure 3.** CFD mesh for full WHOI MOBS, View 2.

Figure 4. CFD mesh for UNH GLOBEC 2.1 m discus buoy.

During the meshing process each fluid model was given named boundaries. These names are passed to Fluent where the boundary conditions are specified for the particular simulation. Each model acts like a wind tunnel with a uniform inflow at one end an outflow at the opposite end. The inflow (front) side of the model was defined as a velocity-inlet, with uniform velocity normal to the face and a specified turbulent viscosity ratio of 1. The top and two sides of the model are also velocity-inlets (turbulent viscosity ratio of 1), except with the uniform velocity vector parallel to the faces along the inflow direction (+x). These boundaries represent the far field where the flow is unaffected by the buoy. The bottom of the model was defined as a wall with specified shear of zero in all directions, representing the ocean surface. The last side of the model, opposite the inflow, is specified as a pressure outlet. This outflow contains the boundary condition of zero gauge pressure, allowing all of the air flowing in through the inlet to flow out.

Each of the final runs for both the UNH and WHOI buoys used the same Spalart-Allmaras (SA) solver model and settings. The SA model is a linear eddy viscosity Reynolds-averaged Navier-Stokes (RANS) based turbulence model, known as a one-equation model as it solves one turbulent transport equation. This model was chosen for its simplicity and robustness. In general the SA model requires a viscous grid along surfaces to accurately resolve the boundary layer. However, in Fluent the model will use wall functions when the grid has not been inflated to resolve the boundary layer. The wall functions use the Law of the Wall to evaluate the flow near surfaces. This was an important model choice since we opted for a non-viscous grid.

Each simulation used air as the fluid with a density of 0.0764717 lb/ft^3 (1.225 kg/m^3) and a viscosity of 1.202e-05 lb/ft-s (1.79e -05 kg/m-s), modeled as incompressible. The solver settings were pressure-based with absolute velocity formulation and were steady in time (except one comparison run, see below). The solution methods were the same for all of the runs as well. The pressure-velocity coupling scheme was set to SIMPLE (Semi-Implicit Method for Pressure-Linked Equations) as the Fluent default for steady state pressure based models being solved iteratively. As for spatial discretization: The gradient was set to the Green-Gauss Node Based method as it is more accurate than the default method and recommended by fluent for tetrahedral meshes. The pressure method was set to PRESTO! for increased accuracy accounting for the high curvature inherent in the models. Momentum was set to Second Order Upwind which was a necessity for the tetrahedral mesh and finally, modified turbulent viscosity was left at the default First Order Upwind.

Due to the complexity of the models, the standard convergence criterion of monitoring the equation residuals was inadequate. Instead, the approach taken was to monitor the three dimensional velocities at the wind measurement sensor locations separately for convergence - this in addition to the residuals. In most cases this involved waiting for the velocities to level out to within four decimal places. In some instances the velocities would oscillate about a central value. As a general reference the coefficient of drag in the flow direction was monitored, as it leveled out, for an indication of convergence imminence. The majority of simulations converged at between 3000 and 4000 iterations. Depending on the complexity of the mesh involved these runs took between 12 hrs and 3 days. Another factor affecting the run times was the under-relaxed factor settings. Under solution controls in the Fluent solution settings menu, the factor for pressure was lowered from the default 0.3 to 0.2 and momentum was lowered from 0.7 to 0.5. These factors were changed to keep the solution from becoming unstable with increasing

viscosity ratio issues. The result was a more stable solution, but also most likely a longer convergence time.

Although all of the final runs were completed in steady state, the first run attempted (UNH Full Model) used a transient solution. This solution ran for over 8000 iterations and 5 days at 2 iterations per adaptive time step. The horizontal velocity pre-convergence value for this run was U = 8.479 ft/s and dropping. The same number for the converged steady state version of the run was U = 8.440 ft/s. The two numbers are approximately 0.5% different off of the inflow velocity of 8 ft/s. Due to the run time difference and the similarity in the solutions, we decided to run all of the other simulations in steady state.

The inflow velocities for the simulations were standardized for each buoy, 10 ft/s (3 m/s) for WHOI and 8 ft/s (2.4 m/s) for UNH. These velocities were chosen more or less arbitrarily under the assumption that the flow characteristics are independent of the flow velocity for the relevant range. A comparison test was done using the full UNH model run at 8 ft/s and additionally 12 ft/s (3.7 m/s). The results for the 8 ft/s run showed flow acceleration (percent difference from inflow velocity) at the sensor location of 5.5% both horizontally and vertically. The 12ft/s run showed 5.3% horizontal and 5.4% vertical flow acceleration. Since the two runs were within 0.2% in both directions it was decided that the assumption was correct and the standard inflow velocities were used for the remainder of the runs.

3. Results

The following discussion of simulation results is organized around individual runs for each of the two buoys examined in our study. In total there were eleven runs, six for the WHOI MOBS platform (henceforth WHOI buoy) and five for the UNH GLOBEC 2.1 m discus platform (henceforth UNH buoy). Each run was developed to evaluate likely important aspects of the flow around the buoy wind sensors. Project time limits as well as the computational time needed to mesh and complete runs also factored into the selection of runs.

The CFD runs for the UNH buoy include three evaluation runs and two runs for sensitivity assessment. All runs were done using the full buoy model as described in Sec. 2. Sensitivity runs were done using the UNH rather than the WHOI model because it required significantly less run time.

The five UNH buoy runs consisted of:

- Run U-1: full model with inflow wind angle with respect to the solar panel of 0 degrees
- Run U-2: full model with inflow wind angle of 45 degrees
- Run U-3: full model without the solar panels
- Run U-4: a run using a transient solver routine (for sensitivity assessment)
- Run U-5: a run with varied inflow velocity (for sensitivity assessment)

The CFD runs for the WHOI buoy were done in "pieces" to reduce complexity and thus increase efficiency and allow more cases to be evaluated. Three different simplifications were used. The

7

initial simplification was to remove all instruments on the buoy tower downstream of the anemometers. For runs with inflow wind angle of 0 degrees, the buoy model was cut in half along a vertical plane of symmetry. This is called the half-model. In order to focus on effects relating either to the instrument tower or the foam float and battery well, the upper or lower sections of the buoy, respectively, were modeled in isolation. One control run was done with the full model and all instruments for validation. Inflow velocity was constant at 10 ft/s for all WHOI buoy runs.

The six WHOI buoy runs consisted of:

- Run W-1: half model with inflow wind angle with respect to the vane of 0 degrees
- Run W-2: half model with inflow wind angle of 30 degrees
- Run W-3: lower model with inflow wind angle of 0 degrees
- Run W-4: upper half-model with inflow wind angle of 0 degrees
- Run W-5: full model with inflow wind angle of 30 degrees
- Run W-6: full model with all tower instruments and inflow angle of 0 degrees

The horizontal and vertical velocity flow distortion perturbations at the pertinent wind sensor locations for each run are summarized in Table 1 (UNH buoy) and Table 2 (WHOI buoy). For the UNH buoy the sensor location is the center point of the volume measured by the DCFS (direct covariance flux system) 3d sonic anemometer. The WHOI buoy sensor location is the center of the face of one or both (left and right) of the anemometer nose cones (this position assumes that the anemometers vanes are aligned with the inflow direction). The velocity perturbations are given as percentages of the uniform (undisturbed) inflow velocity. For the horizontal velocity (along the inflow direction) the percentage indicates an increase (positive) or decrease (negative) from the inflow horizontal flow velocity. For the vertical velocity, the percentage indicates a variation from zero velocity (positive = upward) as a percentage of the inflow. The results for each run are discussed individually in Sec. 3.1 and 3.2.

Table 1. Velocity perturbations for the UNH buoy CFD runs

Run	Description	Horizontal Vel. (%)	Vertical Vel. (%)
U-1	UNH 0 deg	5.41[#]	5.32
U-2	UNH 0 deg no Panels	4.41	3.34
U-3	UNH 45 deg	5.38	5.30
U-4	UNH Transient	5.38	5.30
U-5	UNH 12ft/s	5.36	5.37

\# The UNH buoy also deploys a 2D Windsonic sensor located ~0.3 m down on the met platform from the 3D sonic. The average horizontal distortion was +6% in the mean flow at this height.

Table 2. Velocity perturbations for the WHOI buoy CFD runs

Run	Description	Horizontal Vel. (%)	Vertical Vel. (%)
W-1	WHOI half-model 0 deg	0.38	17.57
W-2	WHOI lower model 0 deg	2.13	3.03
W-3	WHOI lower model 30 deg	1.87(L),* 2.73(R)	3.57(L),* 2.38(R)
W-4	WHOI upper half-model 0 deg	-0.67	11.81
W-5	WHOI full model 30 deg	-1.03(L),* 3.44(R)	13.68(L),* 15.60(R)
W-6	WHOI full (all instruments) 0 deg	0.59	17.05

* L and R refer to the left (starboard) and right (port) side sensor locations on the WHOI buoy with inflow coming from off angle.

The Appendix includes all of the figures mentioned in Sec 3.1 and 3.2. The figures are labeled by run, with a "U" for UNH and a "W" for WHOI and with numbers corresponding to the run numbers as in the following section. Inflow is always from the positive "x" direction. The UNH buoy is always viewed from the right (looking downstream) while the WHOI buoy is viewed from either right or left in order to achieve the best visualization for a given run. The streamlines are shown for a plane which is parallel to the flow and through the sensor location (the streamlines disappear behind the model because they have left the plane while going around parts of the buoy). The sensor locations are marked by yellow cross hairs – representing the center of the 3D sonic for the UNH buoy and the anemometer nose cone for the WHOI buoy.

Note that the data files created during the analysis were organized to include a folder for each run and archived on a workstation at UNH. These folders include a common set of figures to illustrate the general flow of each run, along with additional views to show specific flow characteristics. Not all of the figures in each run are described below, but they are included in the folders. The CFD output data (in an ascii *.csv format) from each run, including pressure and 3-dimensional velocity, are also included in the data set (for full model space and specific planes accordingly). All work can be reproduced by returning to a ANSYS workbench project file that is dedicated to each model run.

3.1 UNH Buoy flow distortion results

3.1.1 Run U-1: Full Model with 0 degree Wind Inflow Angle

It was assumed that much of the flow distortion on this buoy is due to the four solar panels mounted mid-frame at an angle of 30 degrees from vertical. Run U-1 was chosen as a worst-case scenario with one of the four solar panels facing into the wind. **The simulation resolved a horizontal velocity percentage at the sensor of 5.41% and a vertical velocity of 5.32%.** This result shows an acceleration of the flow in both directions, as would be expected as the flow is directed up and over the front solar panel. Figure U-1a clearly illustrates this effect (the 3D sonic sensor location is denoted by the yellow cross hairs).

The streamlines in Figure U-1a show that the flow is directed upwards at the front solar panel. This tends to set the general motion of the oncoming streamlines upwards. It is interesting to note that the streamlines coming out of the hollow above the panels are much closer to horizontal than near the front panel. This is most likely caused by the flat plate located at the top of the buoy frame where the DCFS body is mounted. Although the dissipative effect of the incoming flow also tends to straighten the flow away from obstructions, it can be seen in the figure that above the plate the flow returns to vertically inclined. This tends to show that the panels are not solely responsible for the flow acceleration at the sensor. Run U-2 addresses this matter by removing the solar panels.

Figures U-1b through U-1e show velocity vectors on the same plane as figure U-1a. The vectors are shown in four images zoomed in on the model from bottom to top. The majority of vertical flow seems attributable to: a) buoy foam, b) the panels and then c) the combination of structures at the top of the buoy. Each of these obstructions directs the flow up and over the platform. Much of the horizontal wind flow distortion at the top of the buoy seems to be from the angle iron at the top of the frame. In our static model configuration this presents a flat plate to the inflow (which is already vertically inclined from the distortions below it).

One means to lessen the impact of these flow disturbances on the 3D sonic measurements would likely be to elevate the DCFS mounting to situate the 3D sonic further above the platform. To determine the possible field results that could be gained by elevating the DCFS, readings of the simulation flow velocities were noted at points above the actual sensor location to determine the corresponding distortion at locations 1.0, 1.5, and 2.0 ft above the present sensor head. The velocity percentages for each height are as follows: (H-horizontal/V-vertical): H = 2.77% / V = 3.73%, H = 2.24% / V = 3.13%, H = 1.98% / V = 2.70%. **Results indicate that flow distortion can be cut by a factor of 2 by raising the sensor by 2 ft.** Although 2 ft may be an unrealistic physical modification, any elevation of the sensor will cut down on the measured distortion. For another view of the flow distortion and points of interactions between the inflow and the model, Figure U-1f has been added to the appendix to show the pressure distribution on the same plane as above.

3.1.2. Run U-2: Full Model with 0 degree Wind Inflow Angle - Solar Panels Removed

This run is the same as Run U-1 except that the solar panels have been taken out of the model. Since the solar panels were determined to be one of the major distortion factors above, they have been taken out to demonstrate their effect as well as the remaining model's effect on the flow. The resulting velocity percentages at the sensor location are 4.41% horizontally and 3.34% in the vertical. This is an absolute magnitude percentage drop of approximately 1% and 2%

respectively from the U-1 results. It is evident from the streamlines in figure U-2a that the flow below the top of the frame is much closer to horizontal. As a result, the upward flow in front of the buoy is generally less than in for Run U-1. **Note that the predicted impact of removing the solar panel on the vertical velocity at the 3D sonic would be similar to raising the sonic by 2 ft.**

As in Run U-1 there continues to be a significant upward disturbance in the flow at the angle-iron (base of the large top sensor mounting plate) atop the buoy's superstructure, this is shown in figure U-2a and figure U-2c. This is most likely the largest cause for distortion at the sensor. Figure U-2c shows views of the velocity vectors at the center of the buoy while figures U-2b and U-2d show the bottom and top respectively. Figure U-2b illustrates the upward velocity caused by the buoy float. This distortion is evident in all of the buoys runs in this study, especially so for the larger WHOI MOBS buoy (see runs W-2 and W-3). The pressure plot in figure U-2e illustrates high pressure developed in front of the angle-iron at the top of the frame.

3.1.3. Run U-3: Full Model with 45 degree Wind Inflow Angle

This run was chosen to compare with the worst-case scenario of run U-1. The idea is that, at 45 degrees, the solar panels are no longer directly in the plane of the sensor and that the top frame members are showing a corner rather than a flat plate to the wind. One thing to note is that at all but one corner there is a sensor (or mount) in the same plane as the DCFS location. The direction chosen includes the object thought to be the least obstructive to the flow (see following figures). The corner with no sensor in the path of the flow was not chosen to give a more realistic representation since only the one lacks an obstruction. With more time, a sampling of all directions around the buoy would have been analyzed.

The observed velocity percentages at the sensor location are 5.38% and 5.30%. Surprisingly these numbers are only slightly lower (0.03% and 0.02%) than those observed in runU-1. It is apparent in figure U-3a that the flow is directed upwards near the solar panels. Although they are in different planes, the solar panels affect the airflow in this inflow plane as well. Figure U-3b illustrates a high-pressure bulge near the panels, and it now also shows high pressure all along the nearly-vertical frame member. So, while the panels are no longer in the plane and the top frame is not presenting a flat plate, the obstruction of the large vertical frame member comes into play while the solar panels continue to play a role. As seen in the figures the sensor mount at the corner may also be playing a role in the flow distortion.

Figure U-3c further illustrates the flow zoomed in and exaggerated due to a slightly off-angle view. **We conclude that the net flow distortion for the UNH buoy will not change significantly if the buoy rotates with respect to the inflow direction.**

3.1.4. Run U-4: Full Model with 0 degree Wind Inflow Angle, Transient Solution

As described in the methods section, a transient solver solution was used in our first-attempt runs. This run took much longer than the subsequent runs, but this solution was retained for assessment relative to the steady state solutions. Other than the transient setting, this run is identical to run U-1. The resulting velocities at the sensor for this run came out at 5.38% and

5.30% respectively for horizontal and vertical. **Both of the transient run results are within 0.03% of those in run U-1, indicating that the steady state solutions provide acceptable simulation.** This difference is well within what was considered to be acceptable and subsequently the steady state solution method was used for the rest of the runs. Figure U-4a shows the streamlines for the flow along a plane parallel to the flow through the sensor location.

3.1.5. Run U-5: Full Model with 0 Degree Wind Inflow Angle, Velocity 12 ft/s

This run, like U-4, is a methods validation run. As discussed in the methods section, all of the UNH runs except this one were simulated with an inflow velocity of 8 ft/s. This run used 12 ft/s in an attempt to confirm our assumption that flow characteristics will be independent of the flow velocity (for the range in question). The resultant velocities at the sensor location are 5.36% and 5.37%. Both of these numbers differ from those in run #1 by 0.05%, which shows that the velocity does not affect the flow characteristics. Because of this, the runs for both the UNH and WHOI buoys were simulated at only one constant velocity. A streamline and pressure plot, figures U-5a and U-5b, are included for this run.

3.2. WHOI Buoy flow distortion results

3.2.1. Run W-1: Half Model with 0 degree Wind Inflow Angle

As described in the methods section, the WHOI buoy CAD drawings and physical structure contains a very large number of surfaces at fine scale. Due to project and computational time constraints, this led to a need to decrease the model mesh in some way. The main simplification utilized in this run was to cut the MOBS model in half along a vertical plane of symmetry. Since the buoy is more or less symmetric about each side of its centerline, a boundary condition was imposed through the center. This boundary was defined as a wall with zero shear. This simplification is based on the fact that a symmetric body with head-on flow will not have flow through its center. This assumption is untrue when shedding occurs near the centerline, but since this is a time averaged steady state solution it should hold true.

With the above simplification, all of the larger sensor parts can be included in the full WHOI buoy model computation with a reasonable run time to convergence. Figs. W-1a through W-1f show the results for 0 degree wind inflow angle. The converged **WHOI buoy velocity perturbations are 0.38% and 17.57% respectively for the horizontal and vertical directions.** The discrepancy between these two numbers is very large, i.e. vertical velocity is significantly distorted relative to horizontal. However, unlike the 3-D sonic on the UNH buoy, the propeller and vane anemometers on this buoy are measuring only the horizontal velocity, where distortion is minimal.

The large distortion of vertical velocity seems to be caused by two main factors. The first factor is the foam hull, or float. As in the UNH model, the float sends the flow upward. The WHOI float is much larger, with more volume and surface area above the waterline, so its effect is magnified. The actual distortion caused by the float will be examined in run W-2, although it is clear from figure W-1a that the flow is sent upwards by the float in front of the buoy. Figure W-1a, showing the streamlines along a plane through the sensor, also illustrates a second major

12

cause of distortion. The object in question is the angle-iron at the top of the front of the frame. Similar to the UNH buoy, this frame member presents a flat plate face to the already vertically inclined flow, diverting the flow upwards just before the anemometer. Figures W-1b through W-1f attempt to further illustrate this effect through closer views of the area in question and via different angles and displays with streamlines and velocity vectors.

A short investigation into possible alternative sensor locations was done using data from this run. The velocity perturbations (again in %) were measured at incremental positions between 2 ft vertically and 1 ft horizontally downstream of the nominal sensor location. The furthest displacement, 2ft up and 1ft downstream, shows a horizontal velocity distortion of 0.19% and a vertical distortion of 7.46%. While only slightly lowering the distortion in the horizontal, this new position lowers the vertical distortion significantly, from 17 to 7 %. Results for all of the positions investigated are included in Table 3, where "Distance up" indicates vertical displacement and "Distance over" indicates downwind displacement.

Table 3. Velocity perturbations at different locations on the WHOI buoy.

Distance up (ft)	Distance over (ft)	Horizontal Vel. (%)	Vertical Vel. (%)
0	0	0.38	17.57
1	0	1.50	10.80
1.5	0	1.35	9.07
2	0	1.26	9.63
0	1	-3.83	13.94
1	1	-1.10	10.10
1.5	1	-0.49	8.59
2	1	-0.19	7.46

3.2.2. Run W-2: Lower model with 0 degree Wind Inflow Angle

This run examines the flow around the foam buoy float (with steel well installed) in isolation from the rest of the buoy. Specifically, this run is meant to determine the distortion effect the float has at the sensor position. While the overall flow seen at the sensor location depends on the sum of all aspects of the buoy, this run is meant to give an idea as to the magnitude of the distortion caused by the float alone. Run W-4 will further investigate this sum of the parts strategy by observing the top of the buoy isolated from the rest.

The velocity distortion percentages for this run are 2.13% for horizontal and 3.03% for vertical. This shows that the flow is horizontally accelerated at the sensor location as it is diverted over the float. In the full model, the distortion caused by the top of the buoy must counteract this horizontal acceleration to bring it to the 0.38% seen in run W-1. The vertical distortion caused by the float is 17% of the total vertical distortion seen in the full model from run W-1. **This suggests that the majority of the vertical distortion seen at the sensor is caused by the top of the buoy.** The distortion caused by the float, although it is only 17% of the total, may actually have a greater effect on the overall flow once combined with the rest of the buoy. This is because the float may give the flow a vertical tendency before coming in contact with the other distortion causing entities, causing the flat plate type objects to send the flow up even more so.

3.2.3. Run W-3: Lower model with 30 degree Wind Inflow Angle

As above, this run examines the distortion caused by the float and well top at the sensor location. The simulation in this case, orients the float 30 degrees of off the inflow direction. The buoy is rotated counterclockwise (looking down from above). The purpose for this run is to investigate the effect the well top has on the flow. The well top is shaped like a rounded off square which at 0 degrees presents the point of a diamond to the flow. At 30 degrees, an orientation which is favored by the buoy in field deployments, the well top causes asymmetric flow and shows more of a flat face to the wind.

Note that for the WHOI buoy at an angle to the wind, the two anemometer locations become distinct relative to the inflow. Thus, there are now two crossed yellow lines in each figure, showing the location of the anemometer nose cones. The two locations are typically described as "port" and "starboard" where aft is defined by the location of the buoy vane. For the CFD runs, the locations can also be described as "right" (port) and "left" (starboard) looking in the direction of flow.

The velocity percentages at both sensor locations are noted to examine the differential caused by the asymmetric flow. The left (starboard) sensor location shows 1.87% and 3.57% respectively for horizontal and vertical directions. The right (port) sensor observes 2.73% and 2.38% respectively. This model shows a differential between the sensors on the order of 1% in the horizontal and vertical directions. The cause of the velocity differential is evident in figure W-3a, which shows the streamlines around the well from above. As mentioned in the methods section this run used a non-viscous grid, in reality the flow should separate earlier behind the well. To fully examine the differential, a viscous grid should be used, so the numbers in this run are meant to be qualitative to show that a differential at the sensors can begin far below at the well. Run W-5 below will examine the overall buoy effect on the flow differential.

It is interesting to note that as the buoy is turned further from the wind it has a tendency to continue to turn until it is broad face into the wind. This can be seen in figure W-3d as the well top has been turned 30 degrees counterclockwise, the high pressure at the left corner and low pressure on the right corner of the leading face tend to force it further counterclockwise. The tower section (vertical struts extending from the corners of the well top) will also contribute to this counterclockwise torque. At the same time the large buoy vane in the full model will tend to force the buoy in the opposite direction. At some point the two forces may reach equilibrium.

14

The force balance between the well top/tower and the buoy vane may be the cause for the buoy's affinity for a 30 degree orientation to the wind, although without a viscous grid to fully define the boundary layers this is only a qualitative observation. Figures W-5c and W-5d from run W-5 also illustrate this effect on the buoy, with the directional vane included.

3.2.4. Run W-4: Upper half-model with 0 degree Wind Inflow Angle

This run is the same as run W-1 except that only the top of the buoy is present in the model. That is, we remove the foam float and well. The purpose of this run, along with the above two runs, is to examine the two main distortion causing aspects of the buoy separately. Figure W-4a illustrates the general flow via streamlines on a plane parallel to the flow through the sensor location. As in run W-1 **the flow distortion caused by the angle-iron at the top/front of the frame is evident** in the figure. The velocity percentages are -0.67% and 11.81% respectively for the horizontal and vertical.   Compared to run W-1 the horizontal velocity has dropped approximately 1%, as less air has been passed upwards without the foam float.   The vertical velocity has dropped, from the result in run W-1, by 5.76%. Since the distortion of the float was only 3.03% this result illustrates that **the distortional effects of the bottom and top of the buoy are not simply additive**. The effects of both combine in a more complicated way to give the net distortion seen in run W-1.

Figures W-4b through W-4e illustrate the distortion at the angle-iron in more detail and at different angles, using both streamlines and velocity vectors. Figure W-4f displays the pressure contour for the run, with the high-pressure zone at the angle-iron clearly visible.

3.2.5. Run W-5: Full model with 30 degree Wind Inflow Angle

This run simulates the full buoy oriented 30 degrees into the wind. The buoy is rotated counterclockwise (looking down from above). The full model was simplified by taking out the sensors behind the anemometers. The velocity percentages were sampled at both anemometer locations. The percentages at the left sensor location are -1.03% and 13.68%, respectively for horizontal and vertical directions. At the right sensor location the percentages are 3.44% and 15.60% respectively. These results show a much larger differential between the two sides than in run W-3, where just the foam float was affecting the flow. This is due to the effect of the asymmetric face that the tower top frame presents to the wind at this angle and to the large directional vane. Figure W-5e illustrates the flow on a horizontal plane at the height of the horizontal frame members at the base of the tower top. **This orientation directs more air towards the right side where there is flow convergence, increasing the horizontal velocity. It also presents the frame corner to the wind in front of the left sensor, leading to a decrease in the bluff body effect, flow divergence and a reduction in horizontal velocity.** As the bluff body effect at both sides is decreased due to the angle, the vertical distortion has dropped approximately 4% and 2%, respectively left and right.

Figures W-5a and W-5b show the streamlines on planes parallel to the flow, through the left and right anemometer locations, respectively. Figures W-5c and W-5d illustrate the flow at a horizontal plane cutting through both the well top and the bottom of the directional vane - the former with velocity vectors and the latter with a pressure contour. As was mentioned, regarding

run W-3, the flow dynamics create forces that tend to rotate the buoy. The vane forces the buoy towards the wind inflow direction by high pressure on one side and low pressure on the other (as seen in figure W-5d). The well, on the other hand, is forced in the opposite direction with high pressure at its leading corner and low behind. As mentioned above, these opposing forces may cause the buoy's affinity for 30 degrees, but without a imposing a viscous grid the forces involved cannot be precisely resolved.

3.2.6. Run W-6: Full model (all instruments) with 0 degree Wind Inflow Angle

The purpose of this run to verify results obtained using simplified model configurations, in particular simplifications made to the buoy tower top where sensors are mounted. All WHOI model runs above used a simplified tower top. For the half-model runs (W-1 and W-4) all instruments were included, but the model was cut in half along a vertical plane of symmetry. For the full model run (W-5) the sensors downstream of the measurement points were removed. These simplifications were necessary due to physical and computational time constraints. Run W-6 was executed with the full buoy model and no simplifications to the tower top as a baseline to compare the simplified runs to. This run went for 2100 iterations and took approximately 6 days to reach pre-convergence. Due to the large run time and the fact that this run would only be used for model verification it was not run to "full" convergence (drag still oscillating in the 3rd-4th digit about a central value). The sensor velocity values at this point are virtually unchanging and are adequate for comparison purposes.

The average values of flow perturbation for the left and right sensors are 0.59% and 17.05%, respectively for horizontal and vertical velocities. **These numbers are within a half of a percent of those seen in the simplified model in run W-1, confirming the validity of the simplifications** at this level of investigation.

16

Acknowledgment

References

Colbo, K. and R. A. Weller, 2009. Accuracy of the IMET sensor package in the subtropics, *J. Atmosph. Ocean. Technol,*. **26**(9), 1867-1890.

Irish, J., D. Vandemark and S. Shellito, 2010. Moored observatories for the study of gas exchange in the coastal ocean, ONR/MTS Buoy Workshop, 9-11 March 2010, Monterey CA.

Appendix: Selected Figures from CFD runs
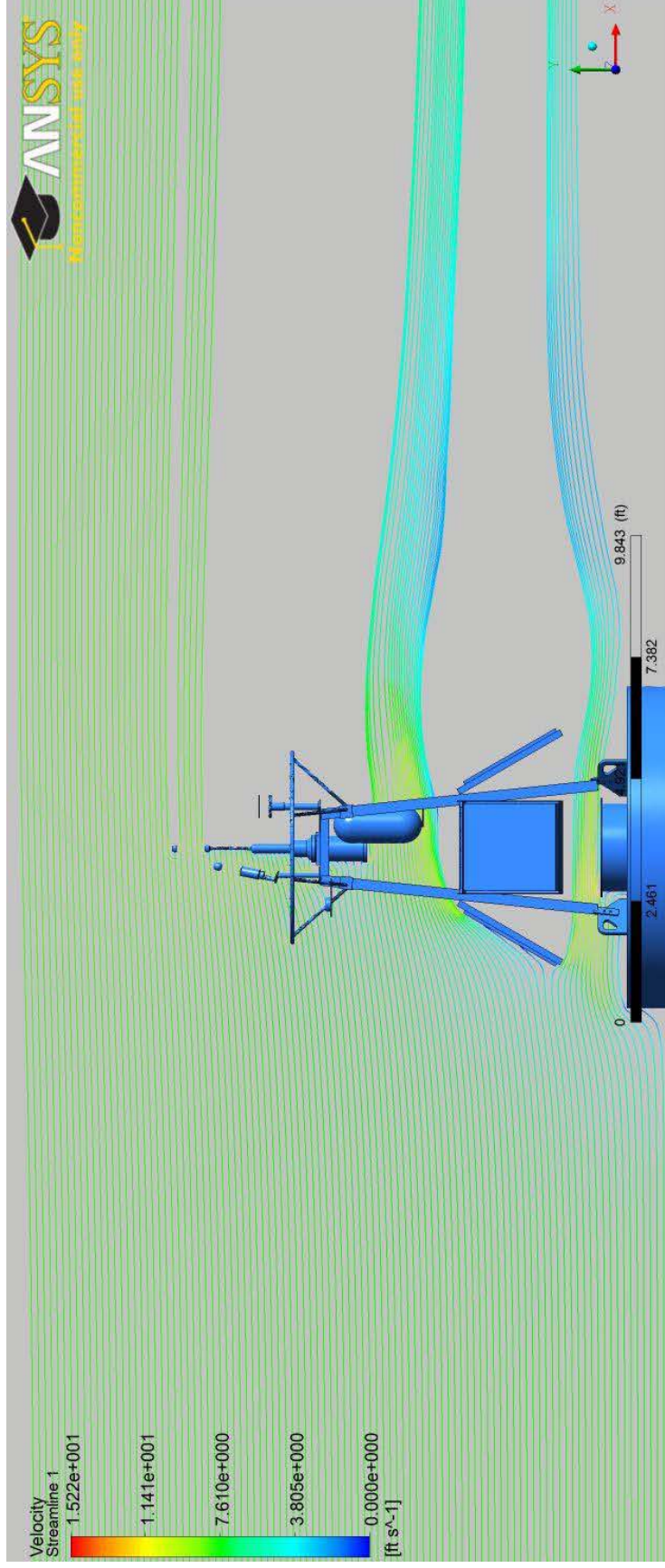
Figure U-1a   UNH 0 deg. wind inflow angle, view 1
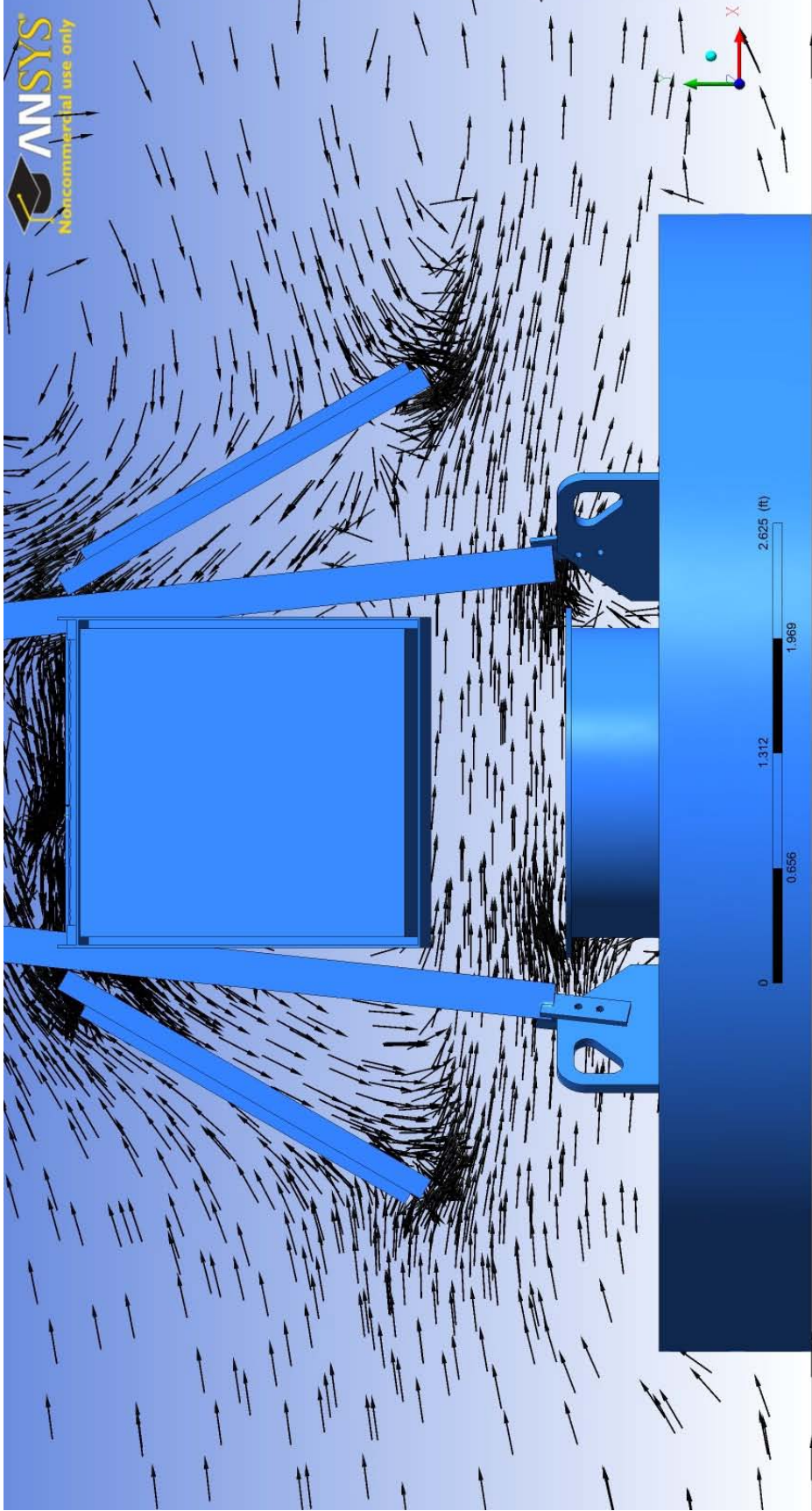
Figure U-1b   UNH 0 deg. wind inflow angle, view 2

19
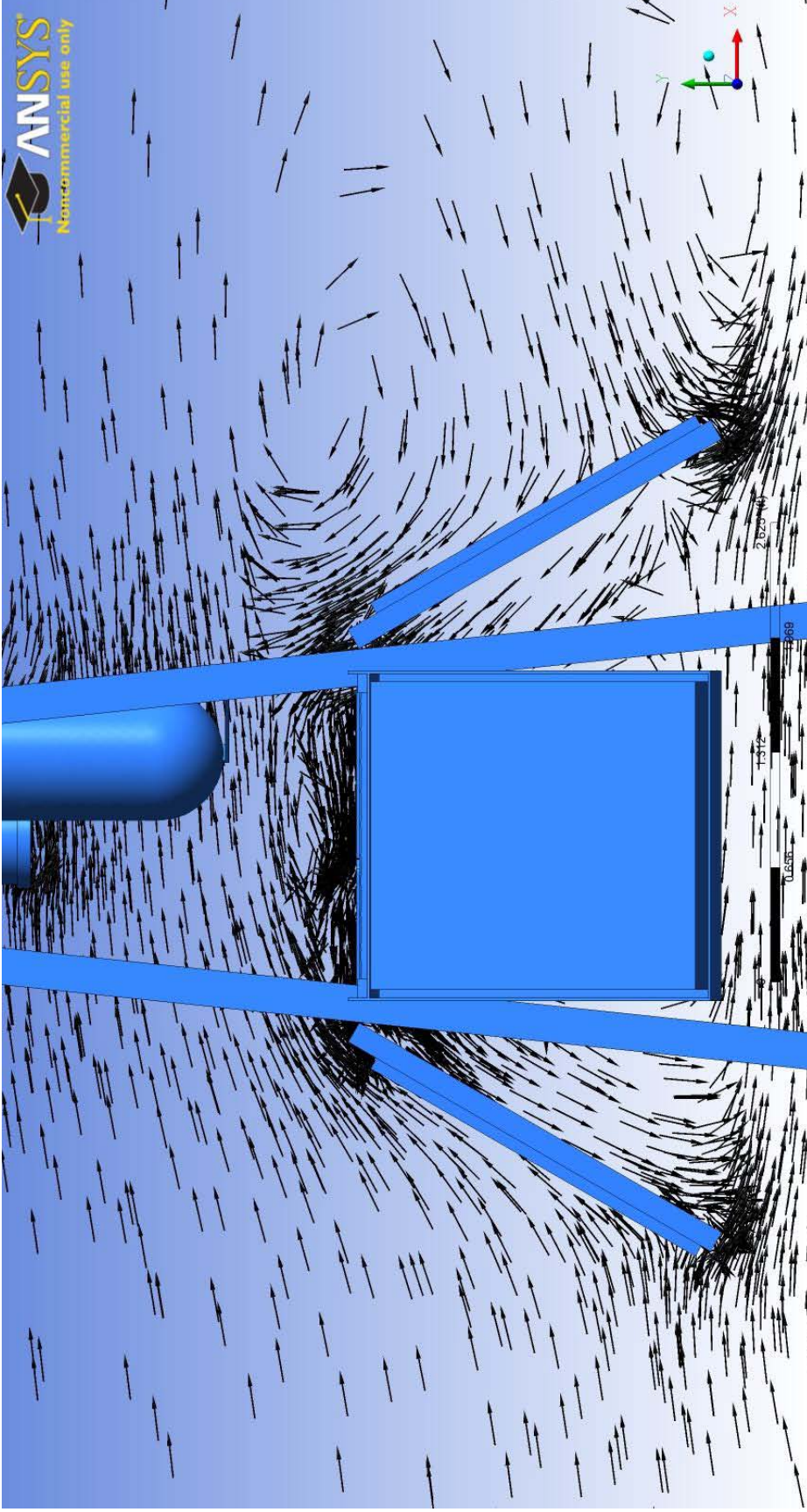
Figure U-1c   UNH 0 deg. wind inflow angle, view 3

20
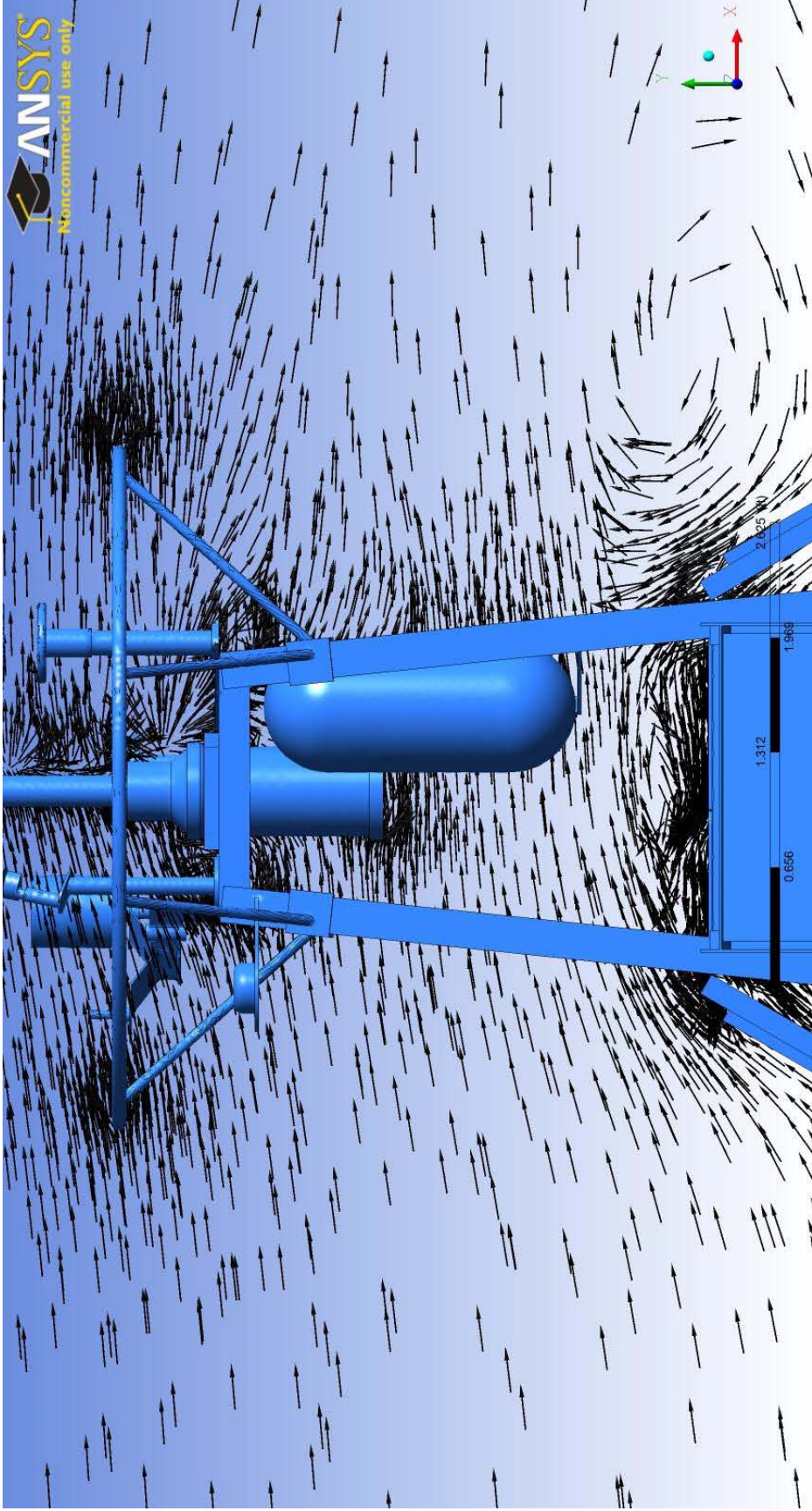
Figure U-1d   UNH 0 deg. wind inflow angle, view 4

21
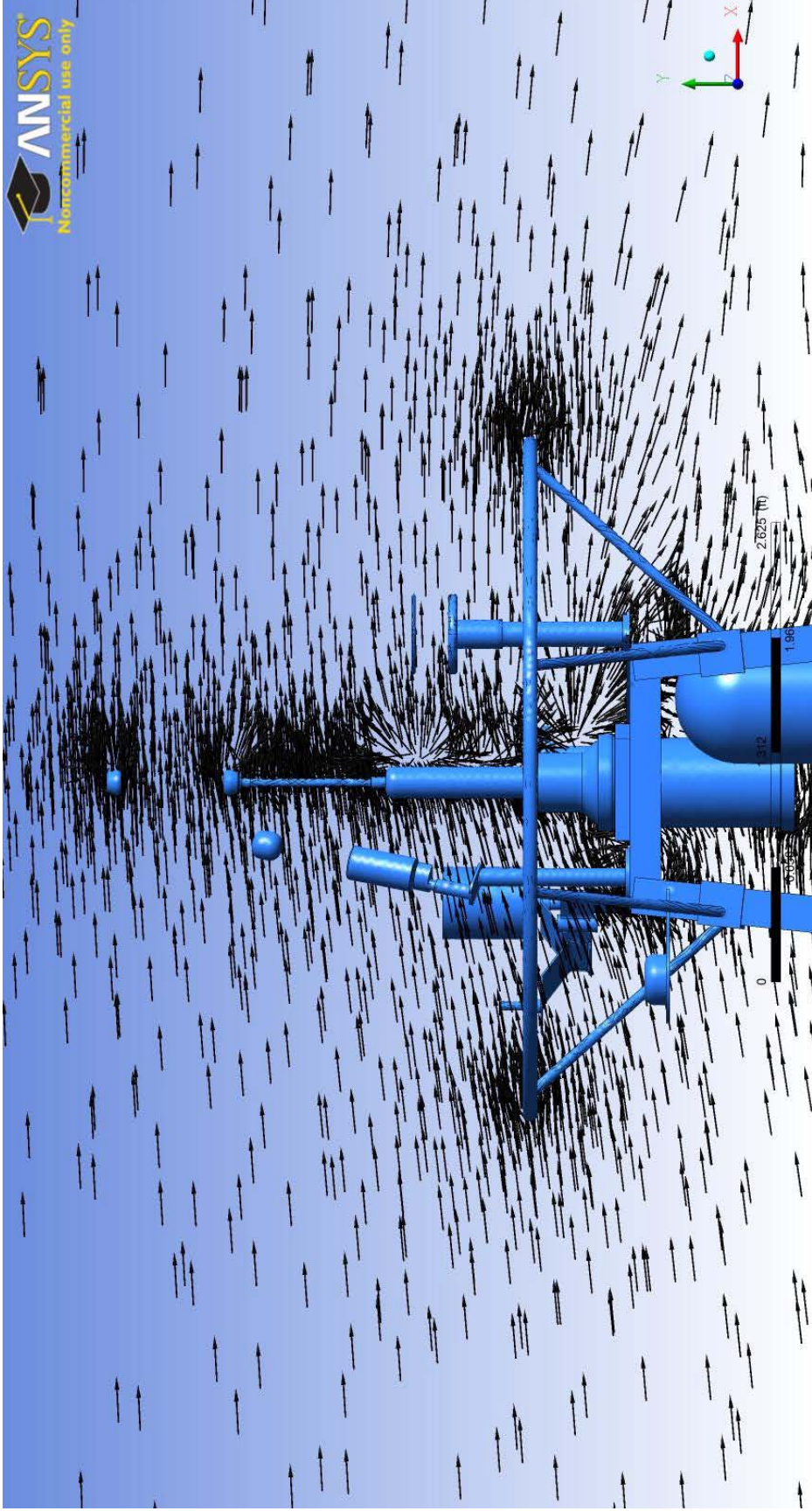
Figure U-1e   UNH 0 deg. wind inflow angle, view 5
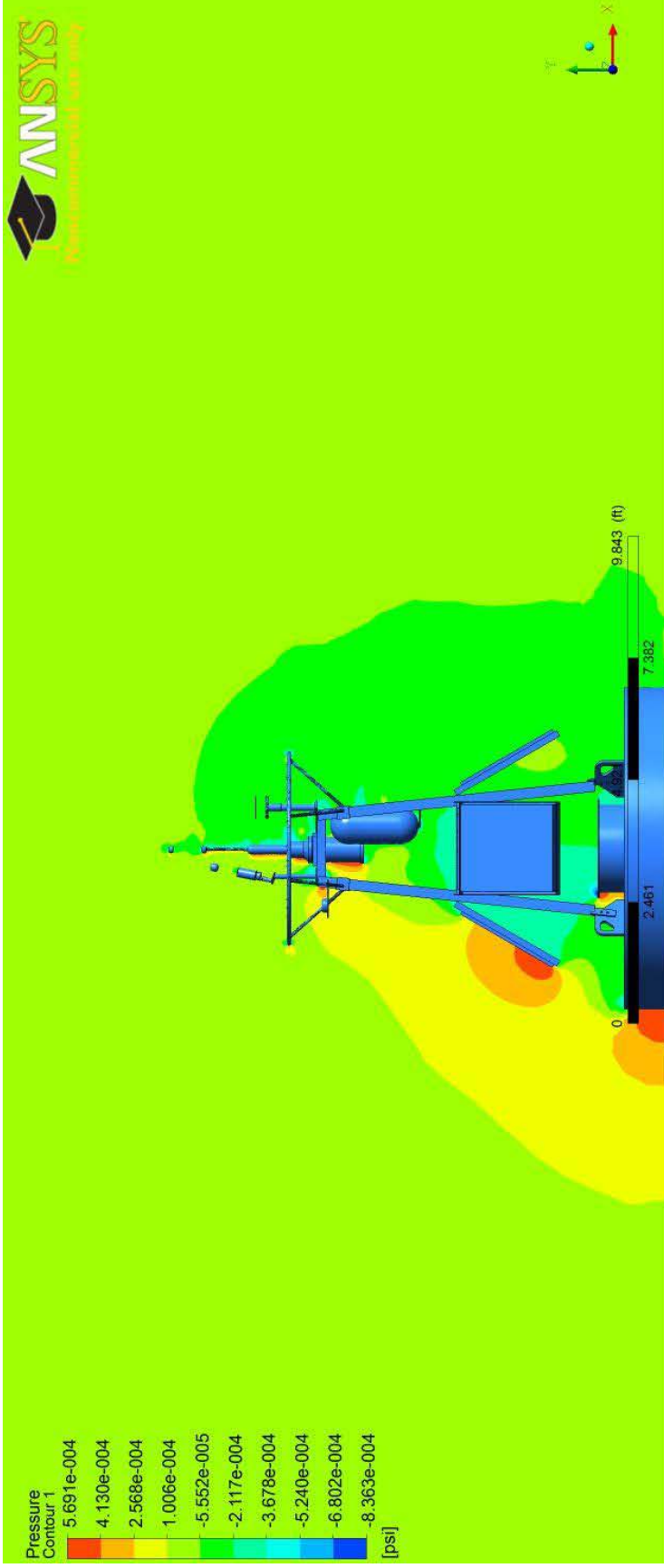
Figure U-1f   UNH 0 deg. wind inflow angle, pressure field
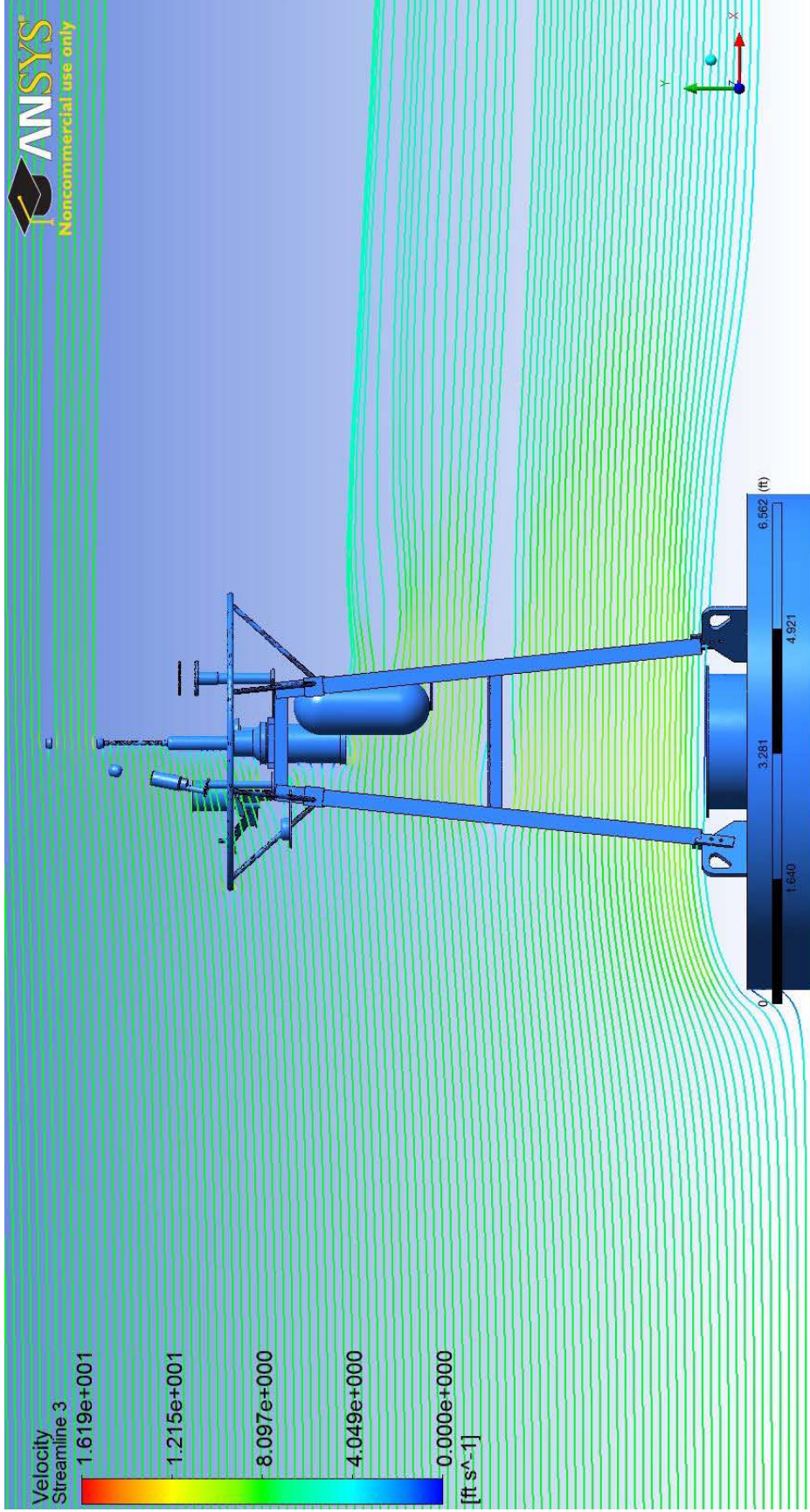
Figure U-2a   UNH 0 deg. wind inflow angle, no solar panels, view 1

24
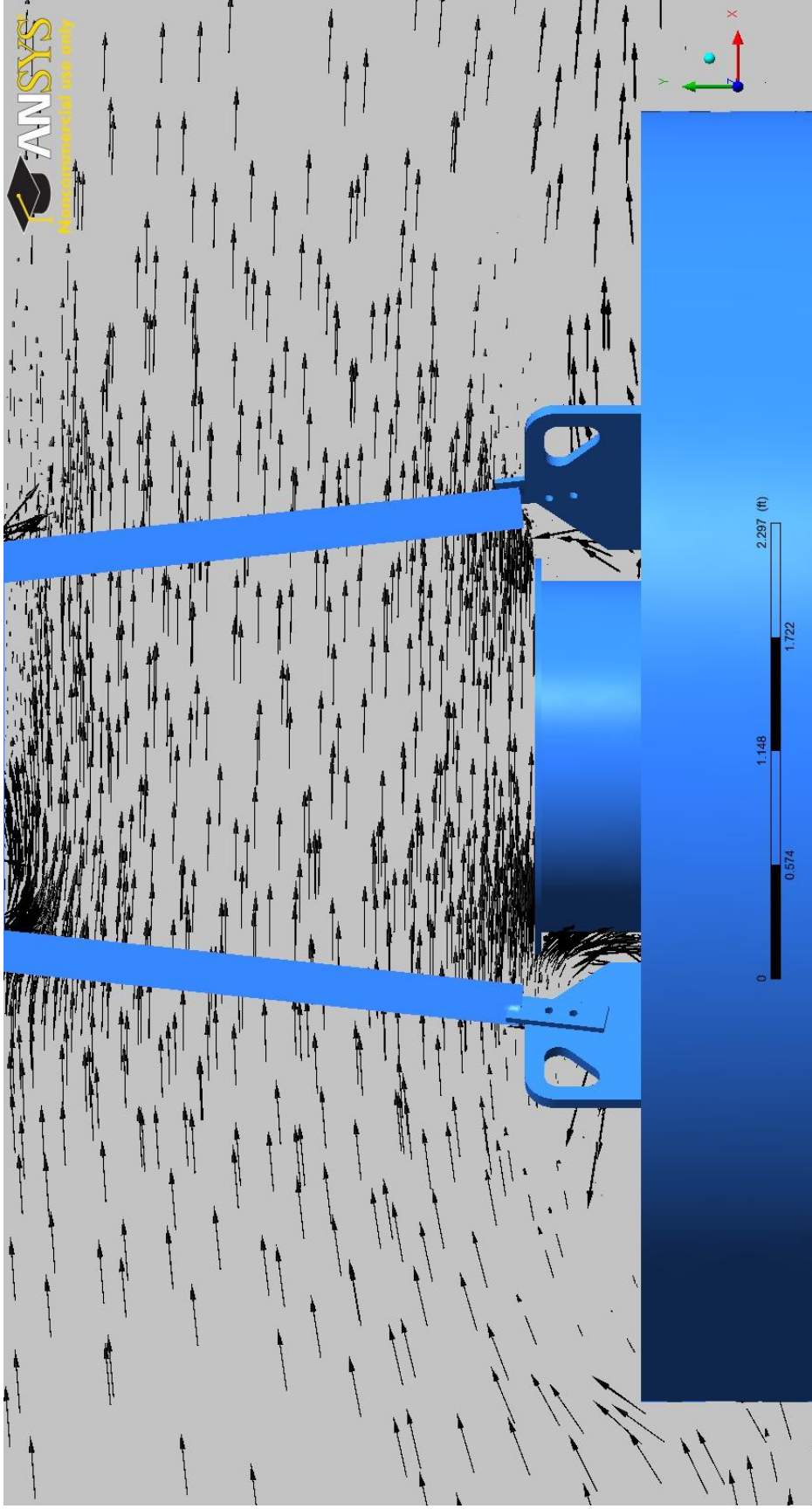
Figure U-2b   UNH 0 deg. wind inflow angle, no solar panels, view 2

25
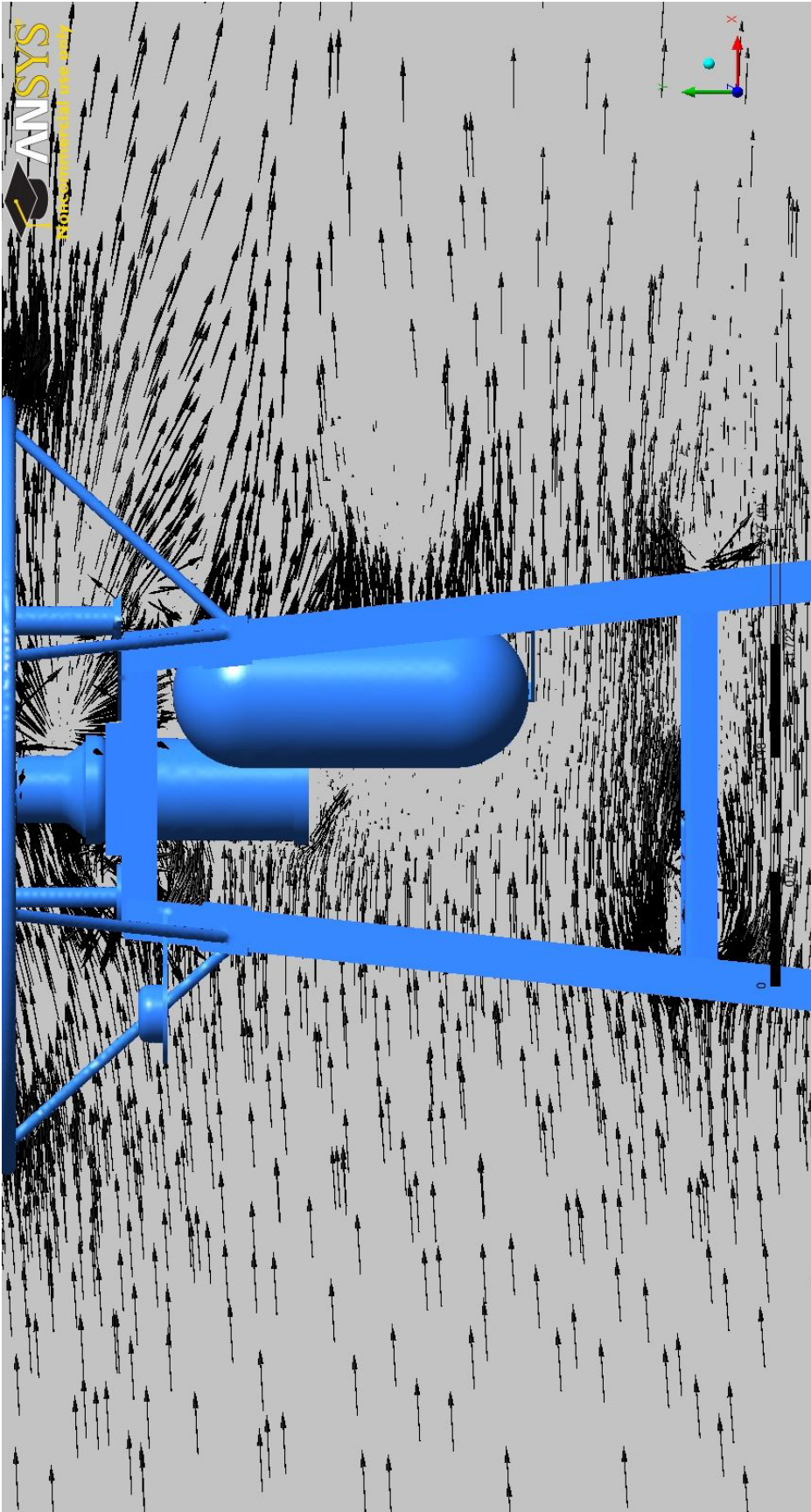
Figure U-2c   UNH 0 deg. wind inflow angle, no solar panels, view 3

26
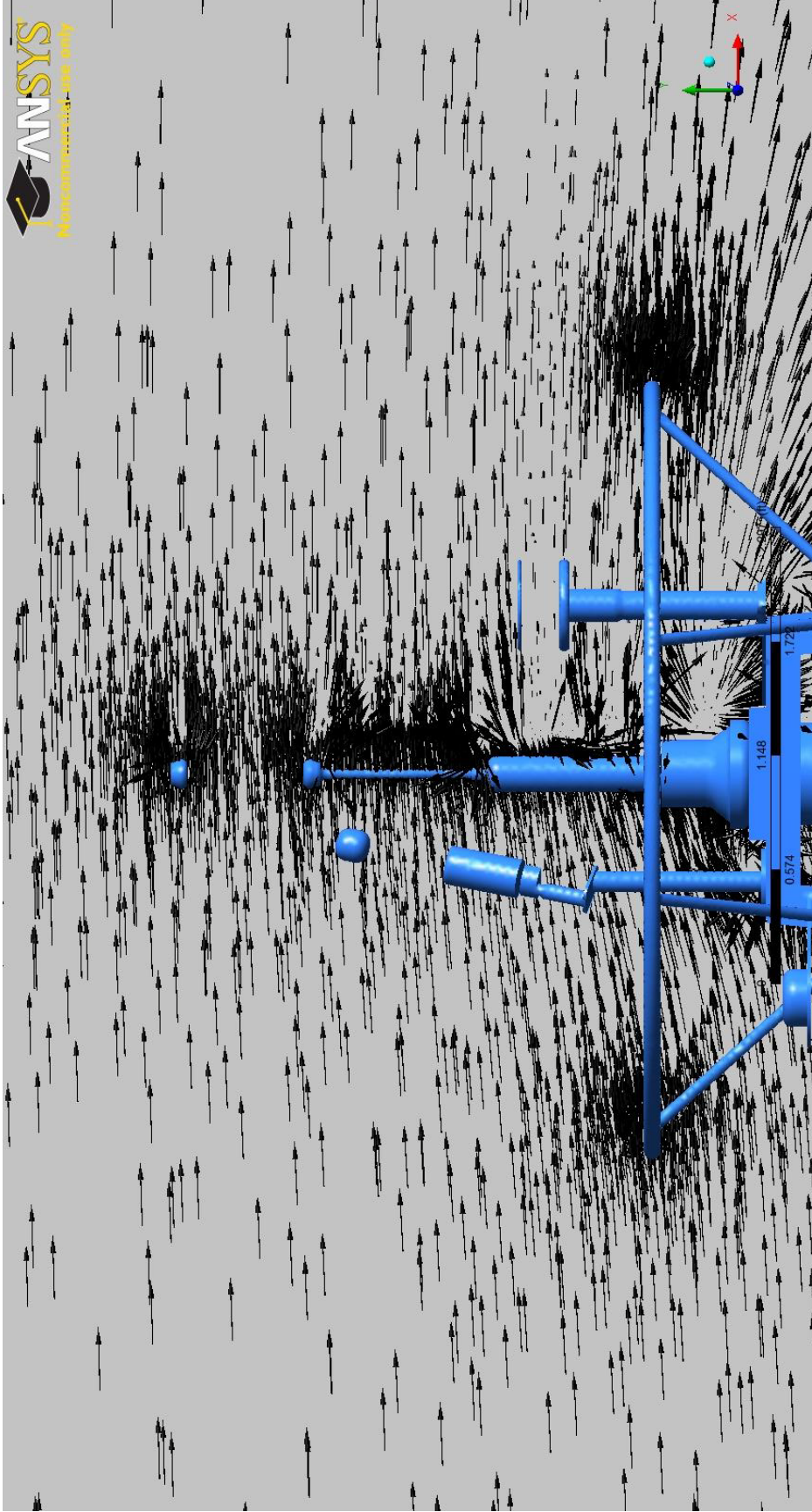
Figure U-2d   UNH 0 deg. wind inflow angle, no solar panels, view 4

27
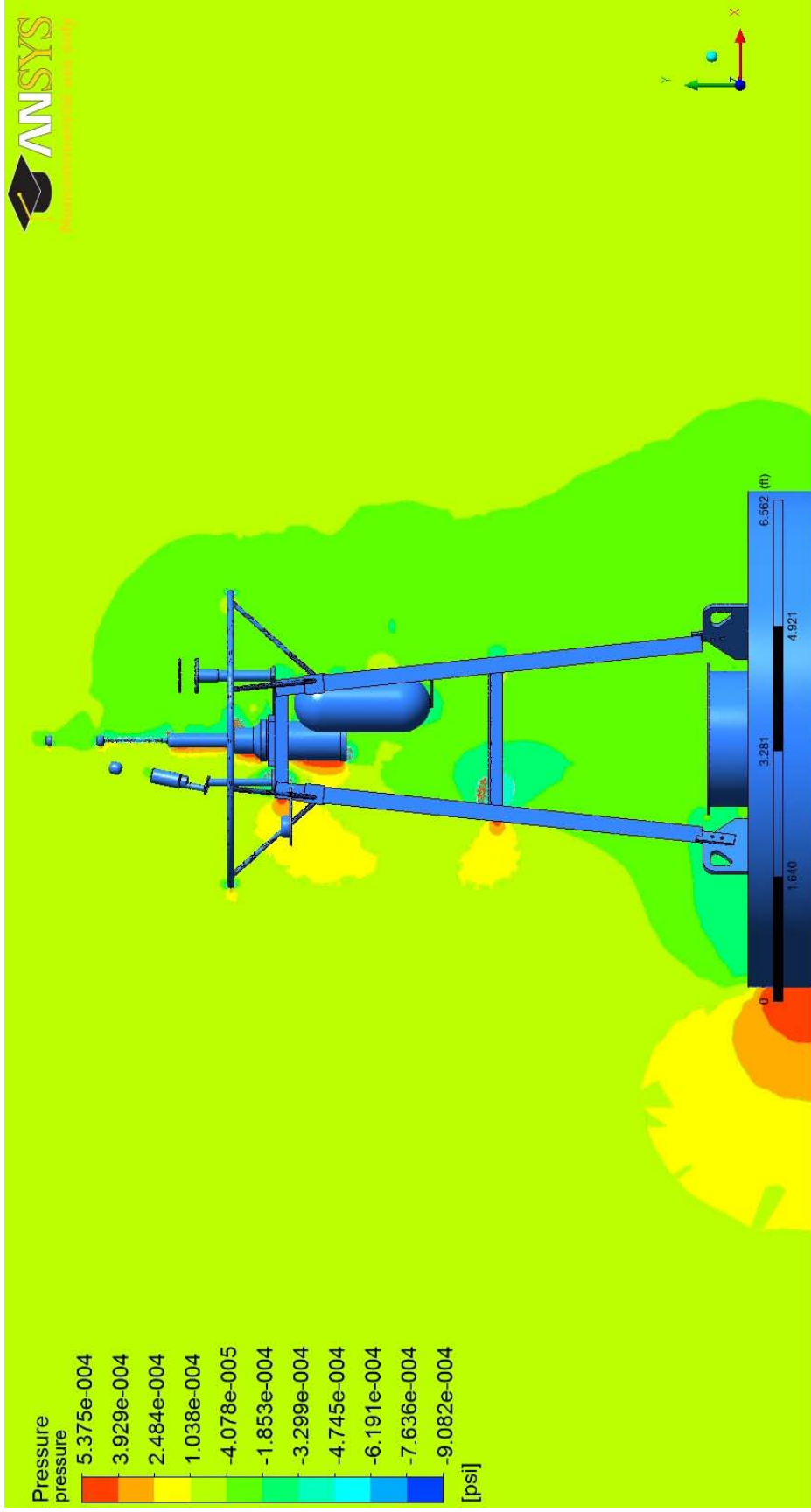
Figure U-2e   UNH 0 deg. wind inflow angle, no solar panels, pressure field
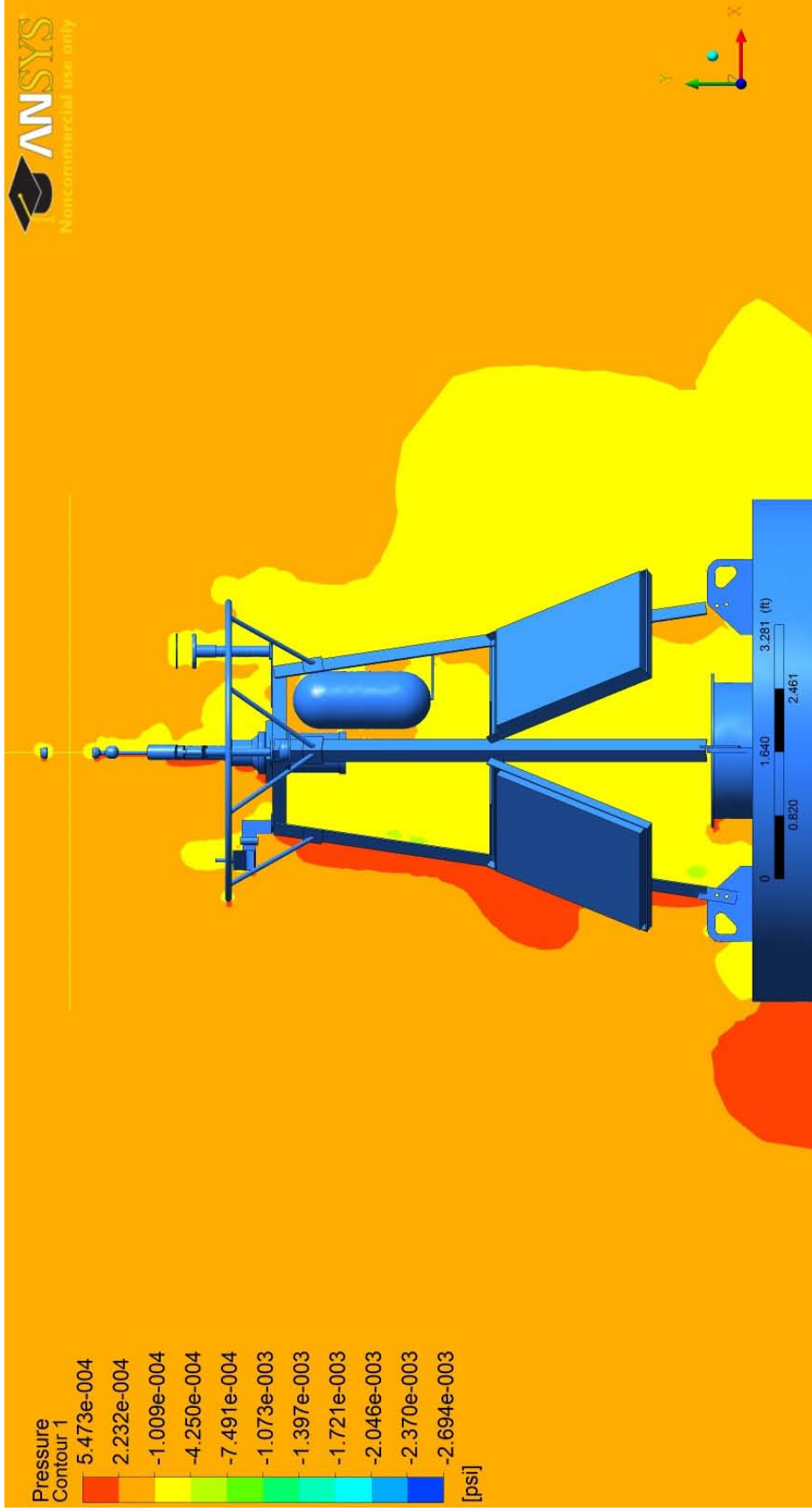
Figure U-3b   UNH 45 deg. wind inflow angle, pressure field

29
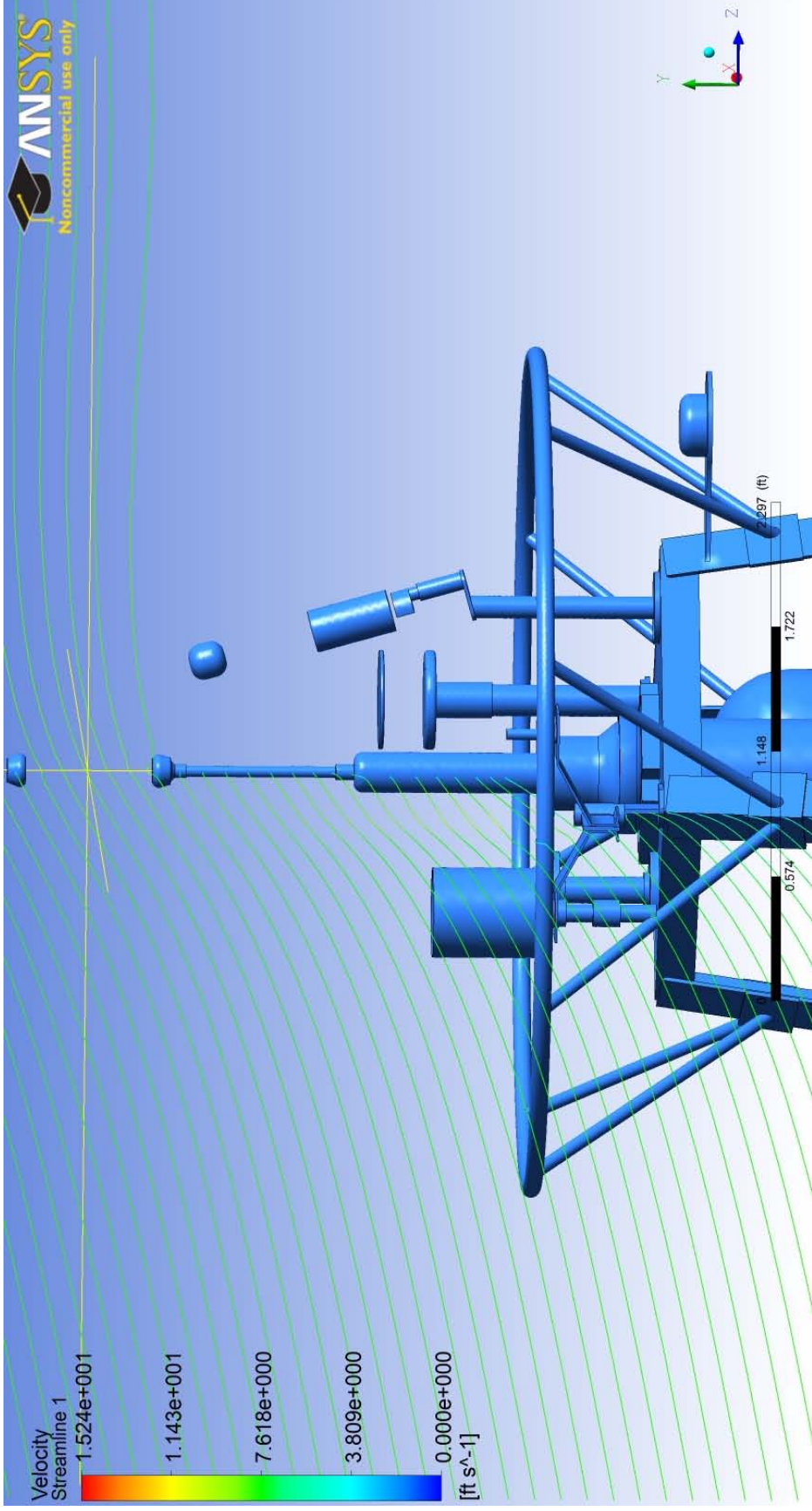
Figure U-3c   UNH 45 deg. wind inflow angle, streamlines
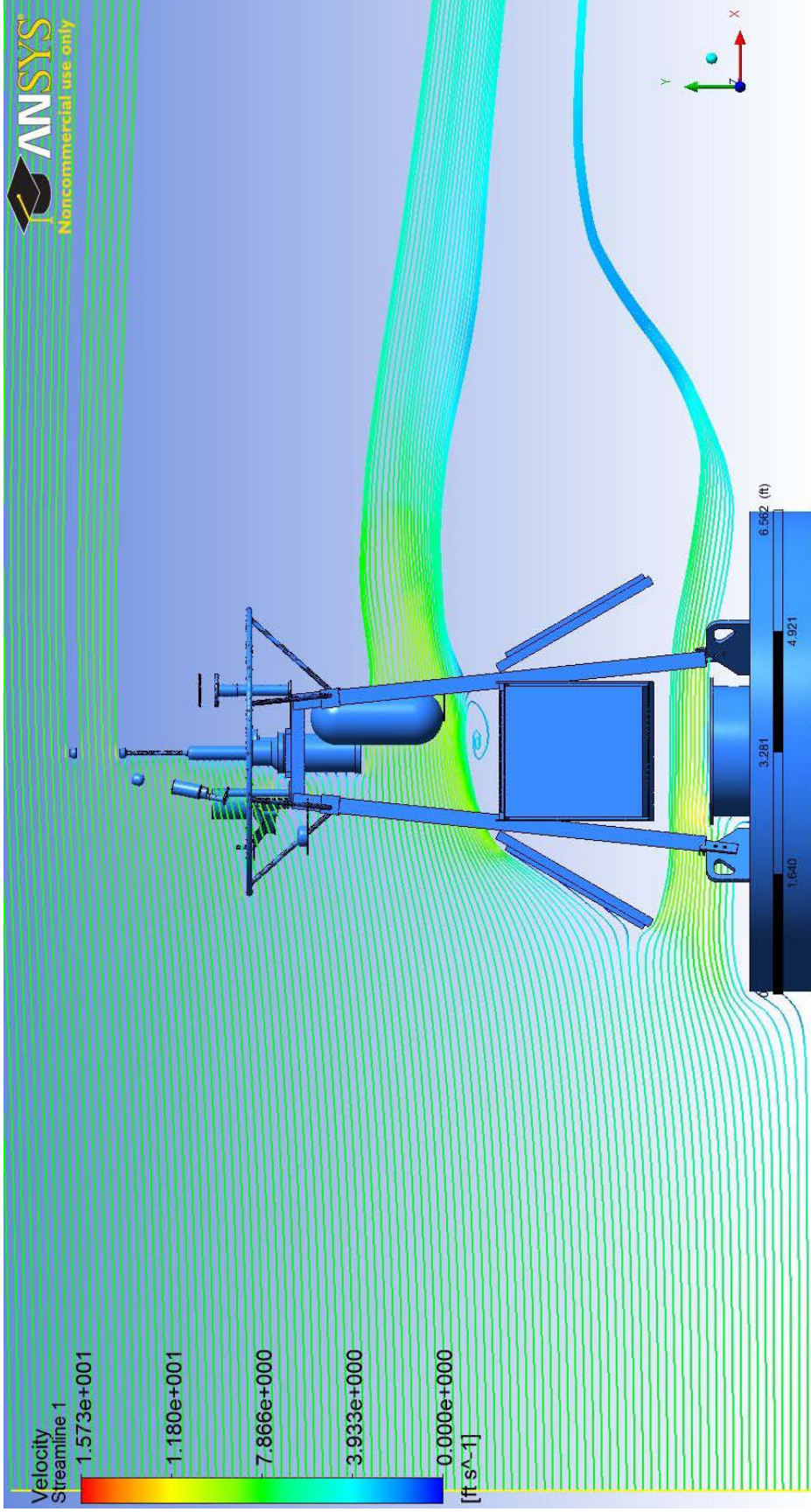
Figure U-4a   UNH 0 deg. wind inflow angle with transient solver, streamlines

31
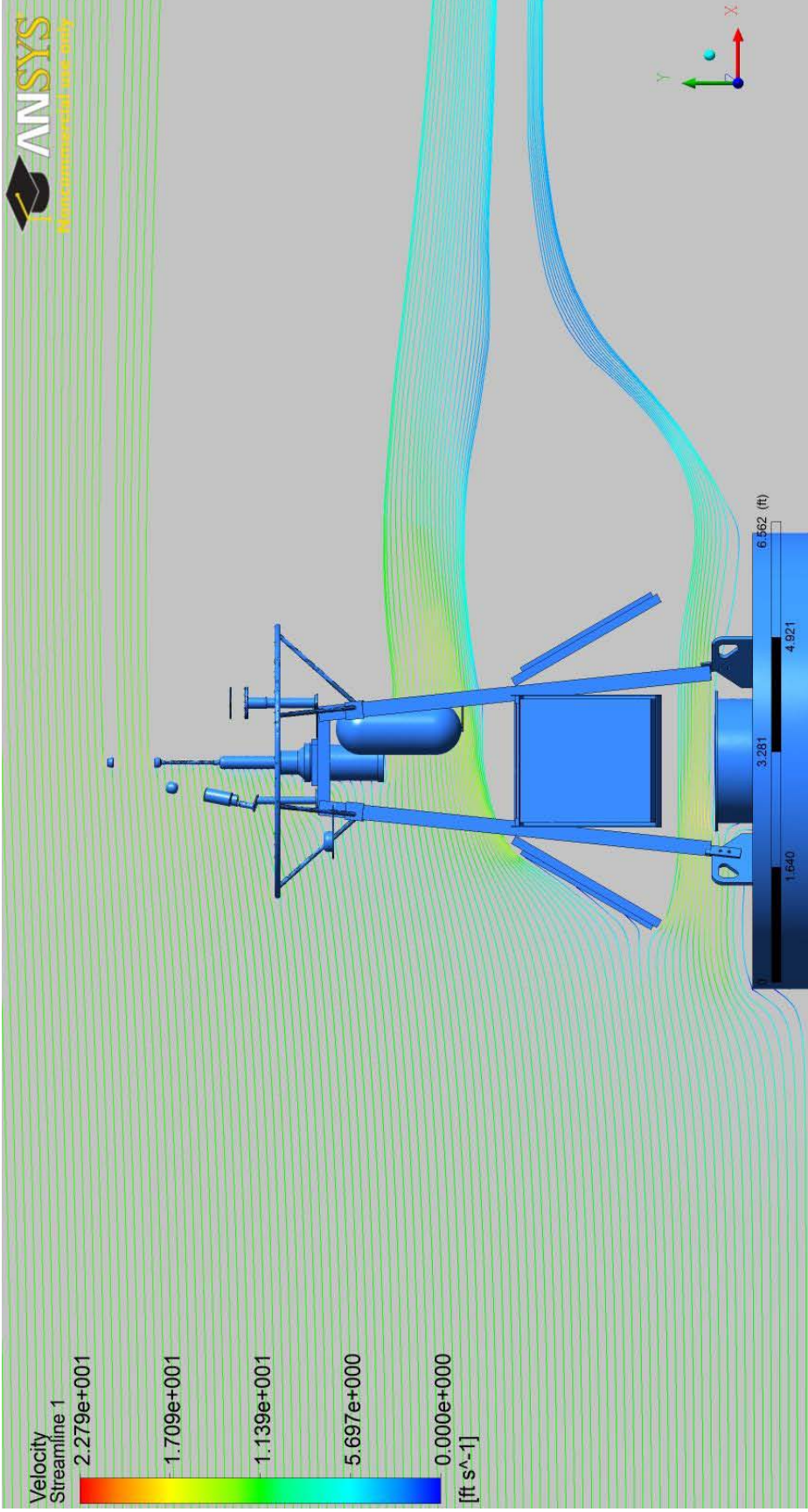
Figure U-5a   UNH 0 deg. wind inflow angle, 12 ft/s velocity, streamlines

32
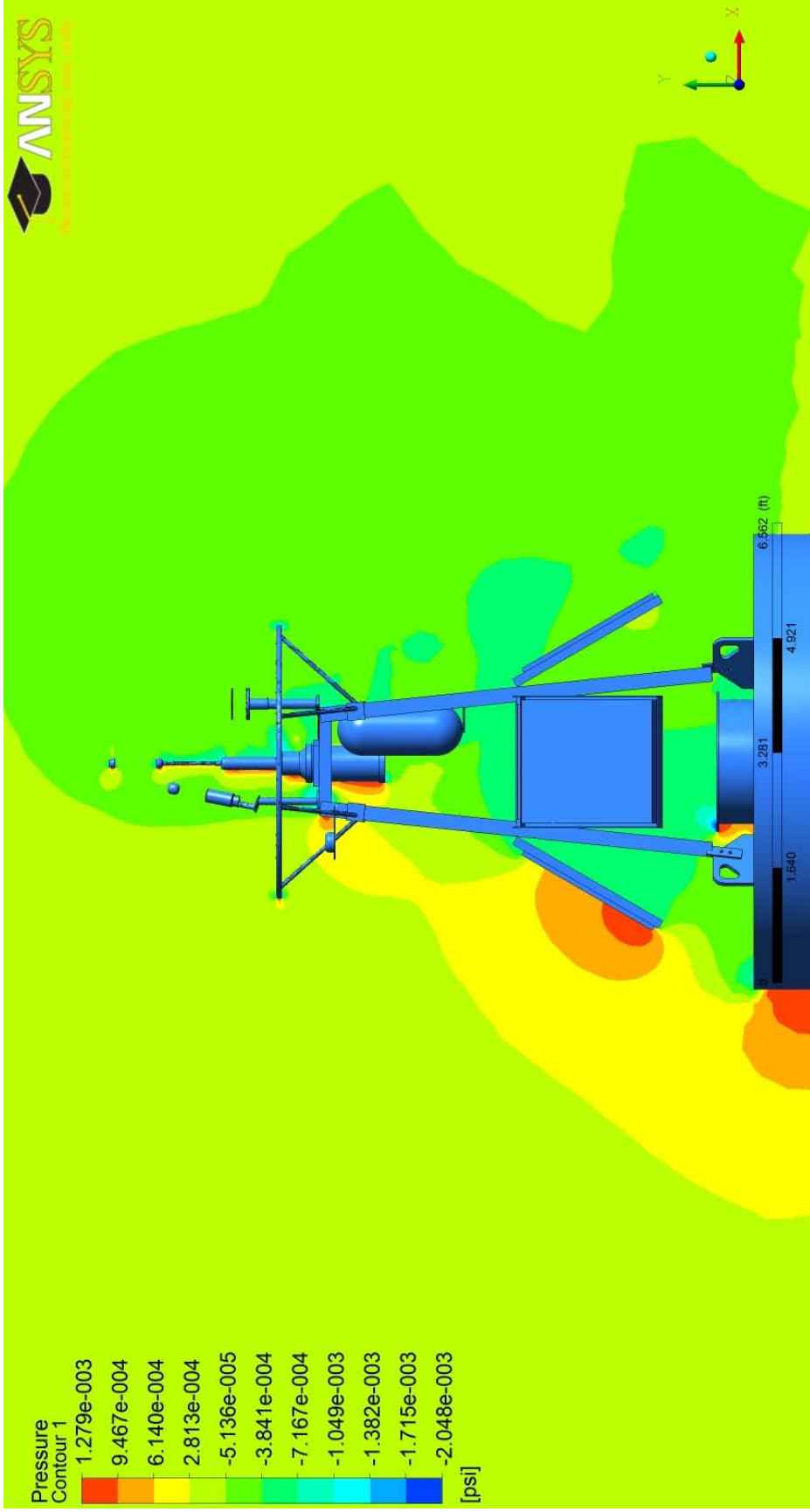
Figure U-5b   UNH 0 deg. wind inflow angle 12 ft/s velocity, pressure field

33
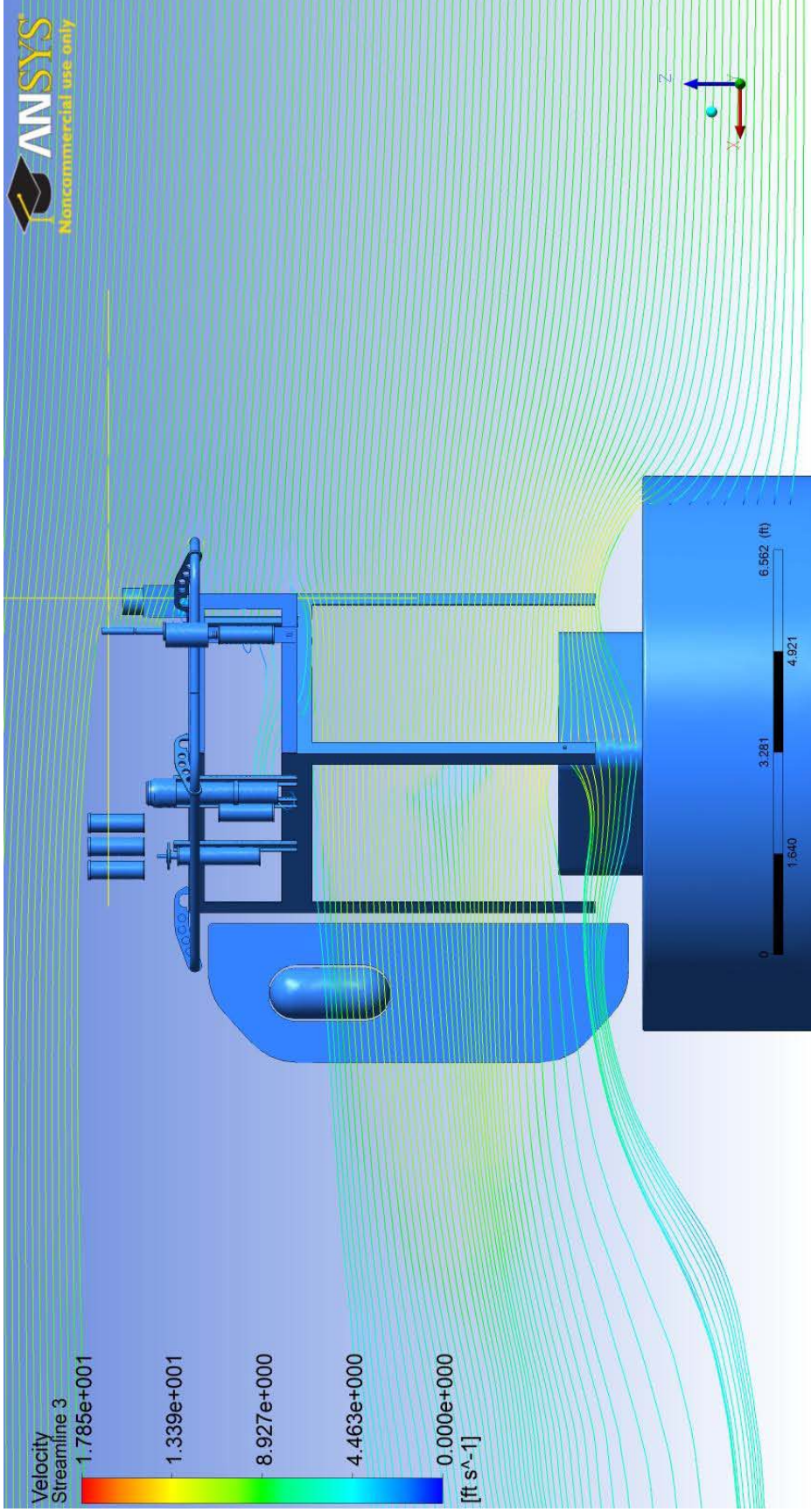
Figure W-1a   WHOI half model with 0 deg. wind inflow, view 1

34
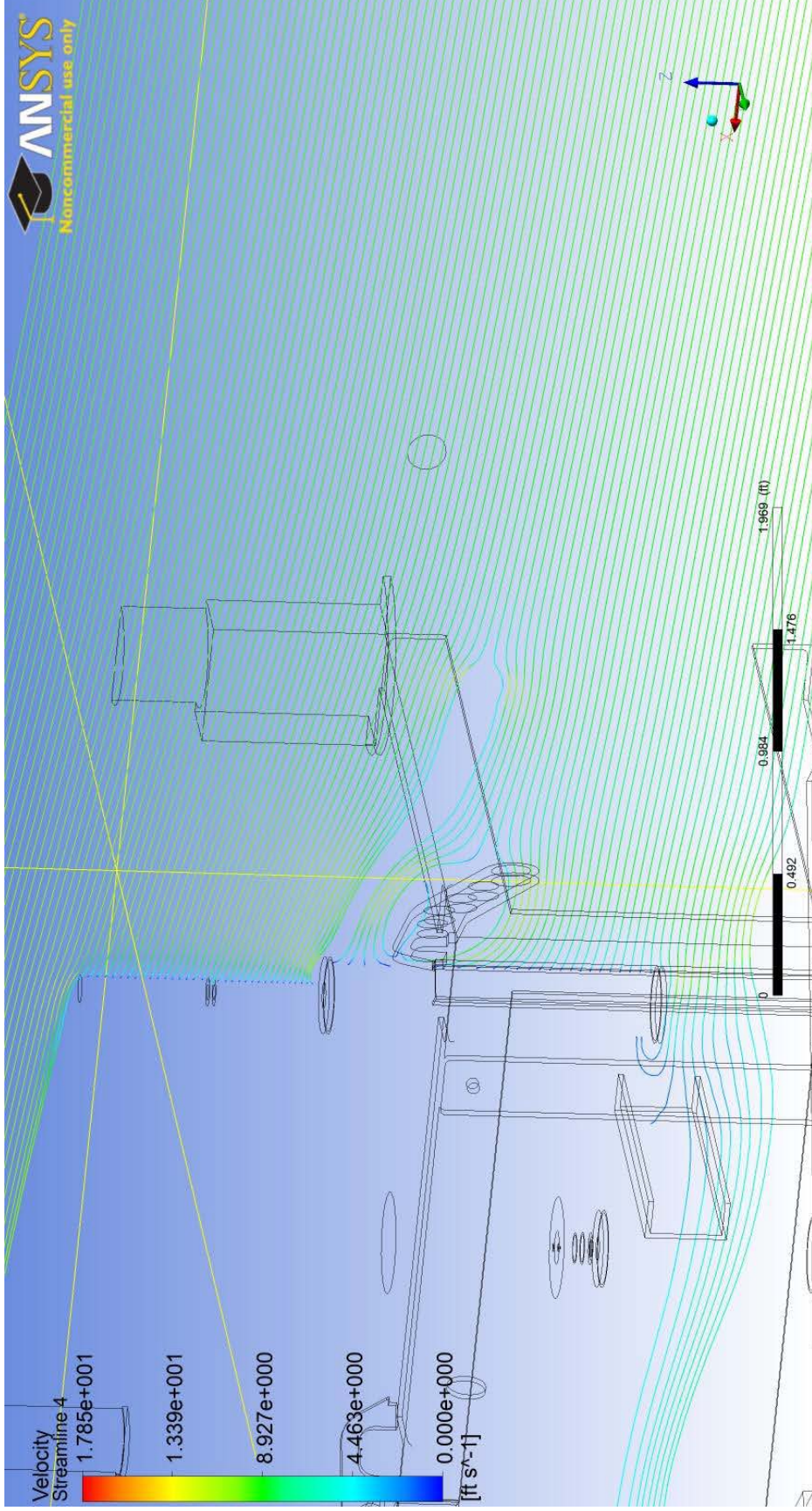
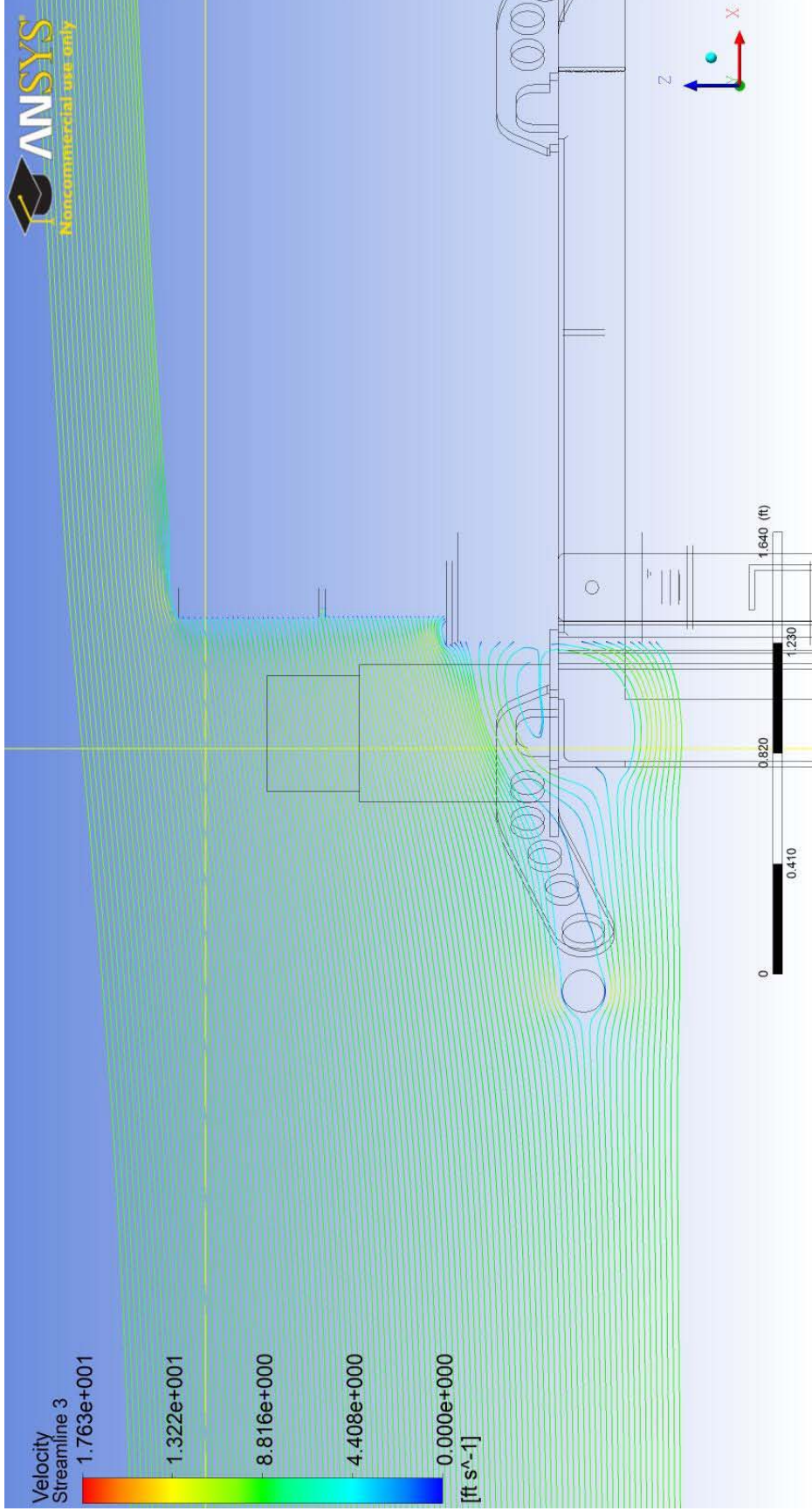Figure W-1b　　WHOI half model with 0 deg. wind inflow, view 2

35
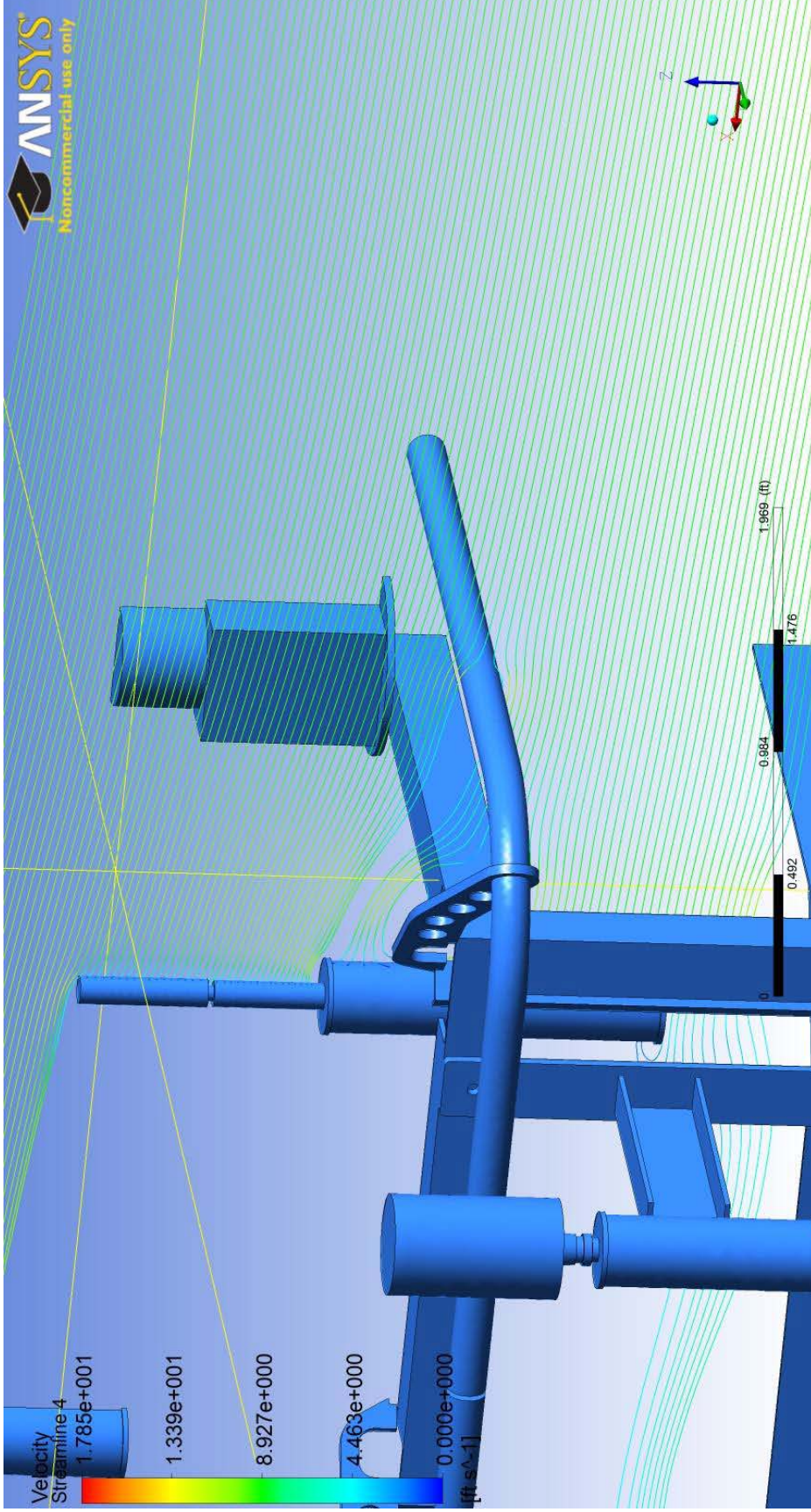
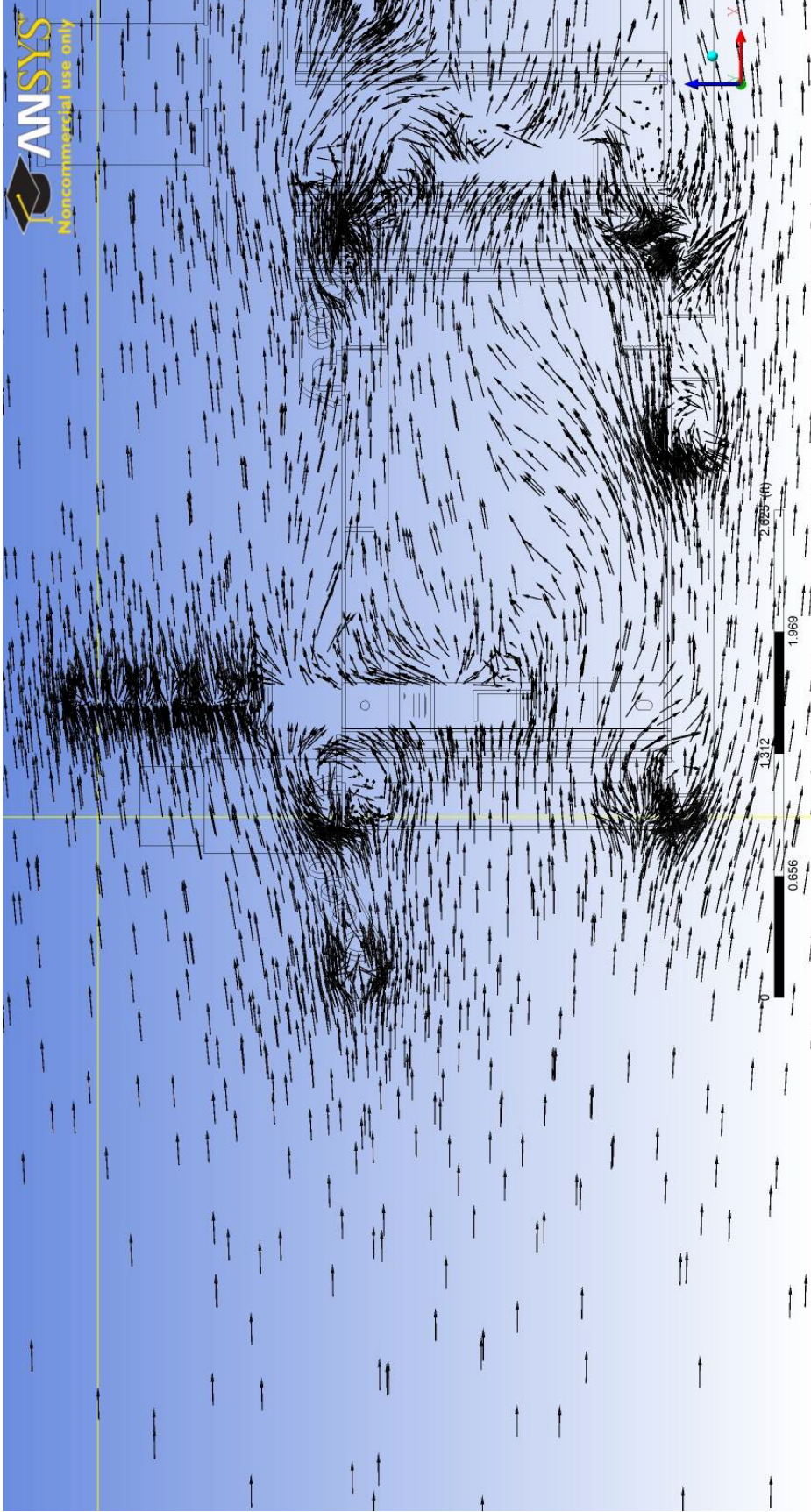Figure W-1c   WHOI half model with 0 deg. wind inflow, view 3

36
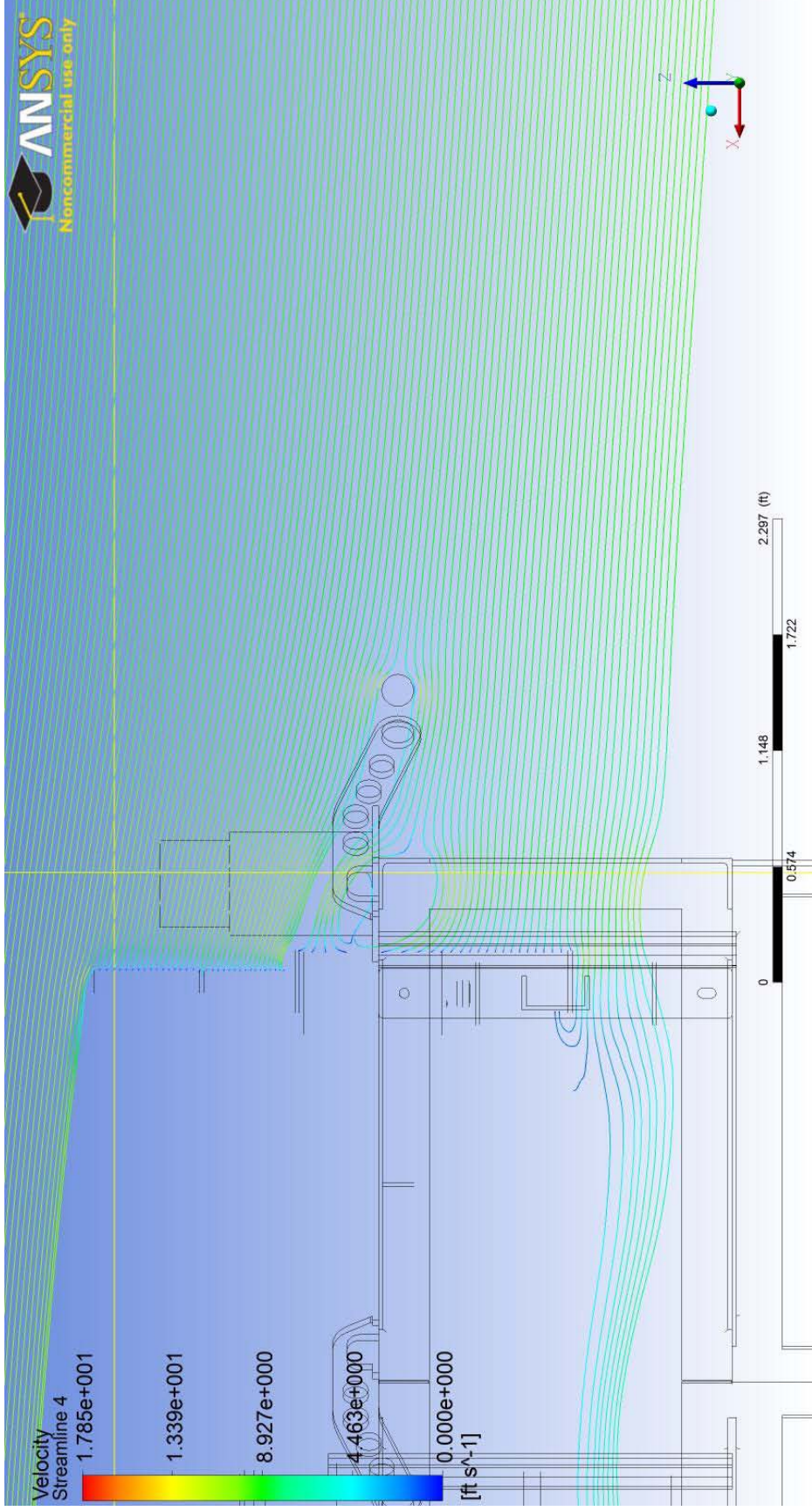
Figure W-1d   WHOI half model with 0 deg. wind inflow, view 4
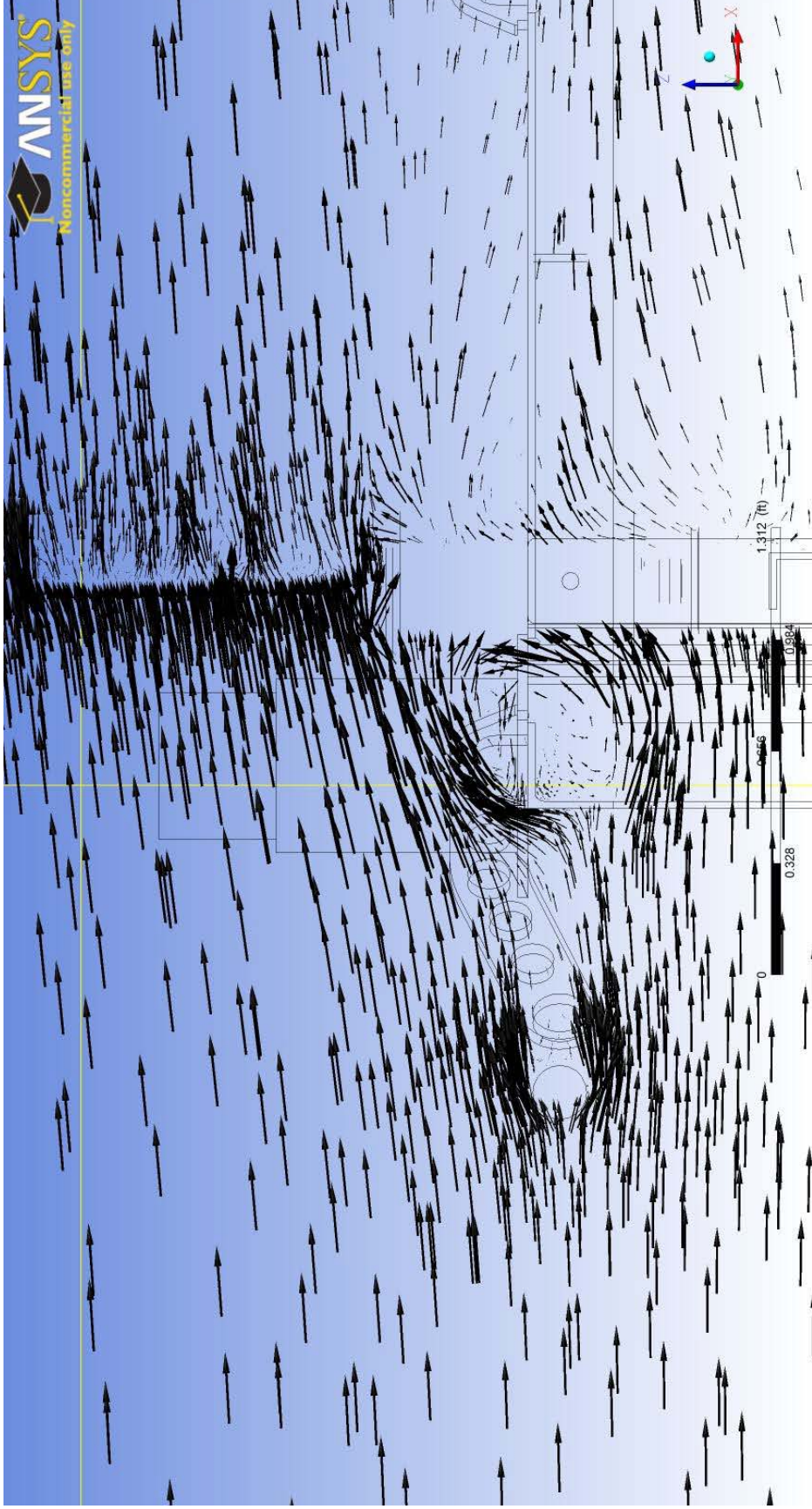
37
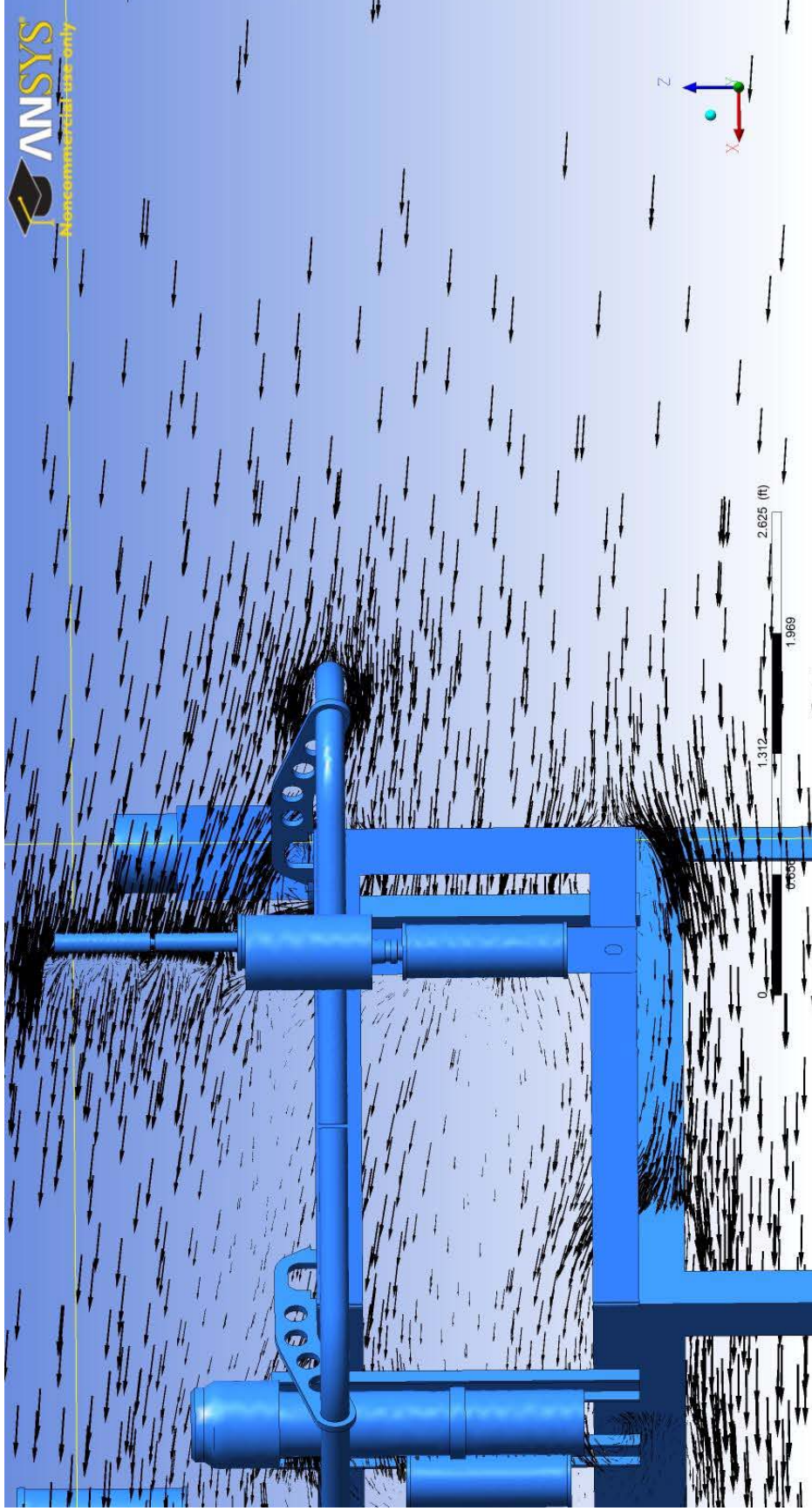
Figure W-1e   WHOI half model with 0 deg. wind inflow, view 5

38
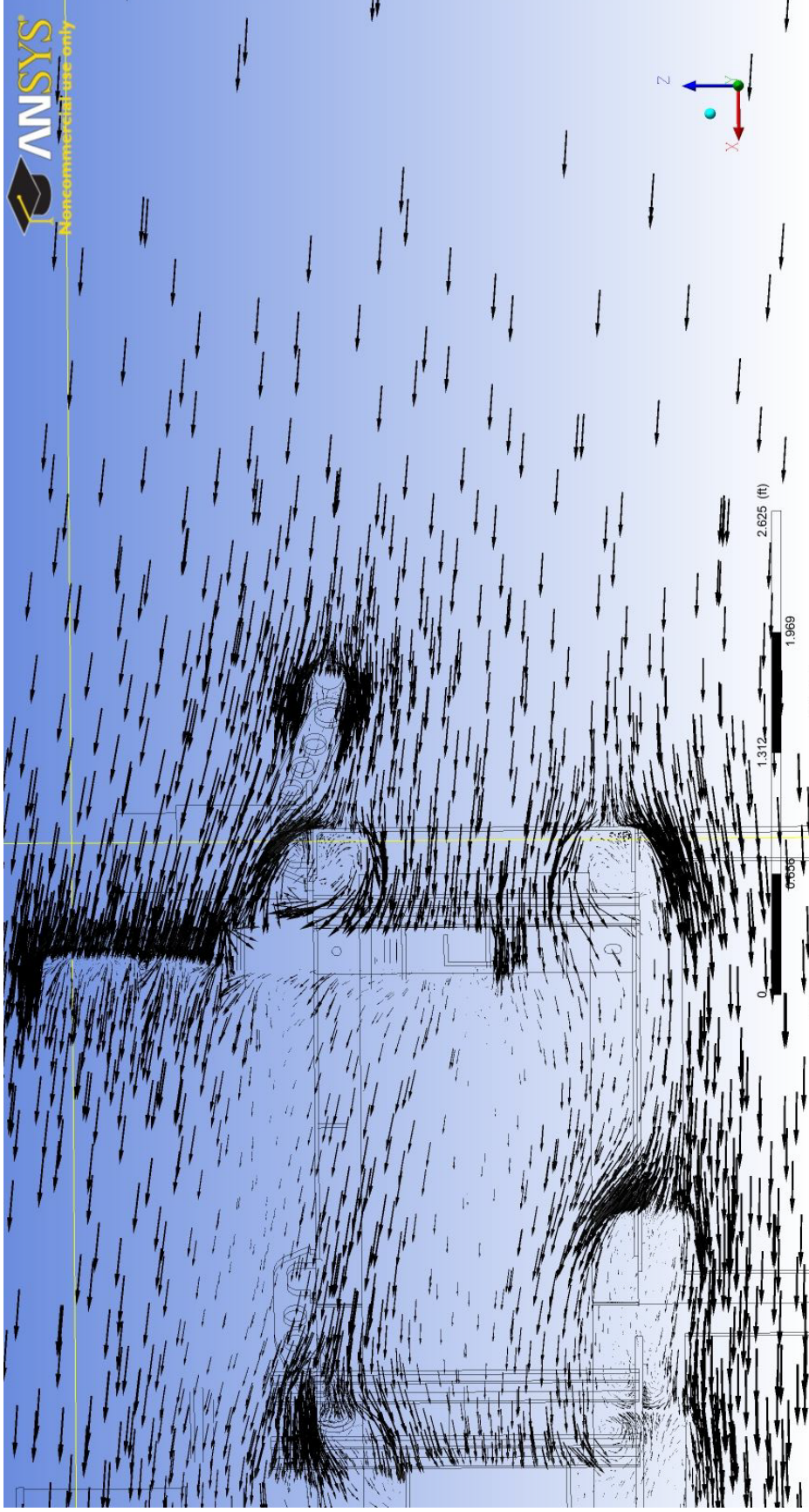
Figure W-1f   WHOI half model with 0 deg. wind inflow, view 6
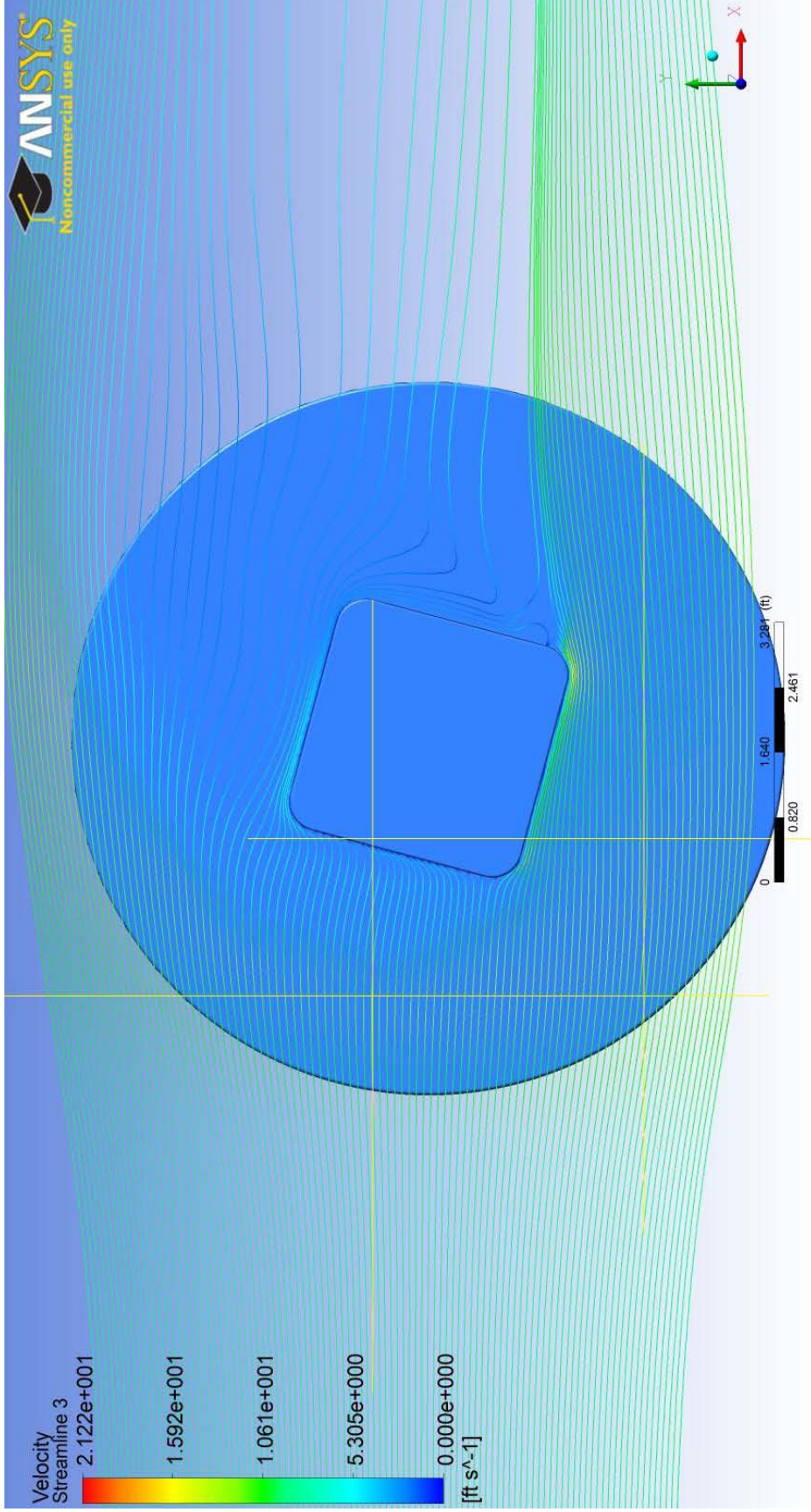
Figure W-3a   WHOI lower model with 30 deg. wind inflow, view 1

40
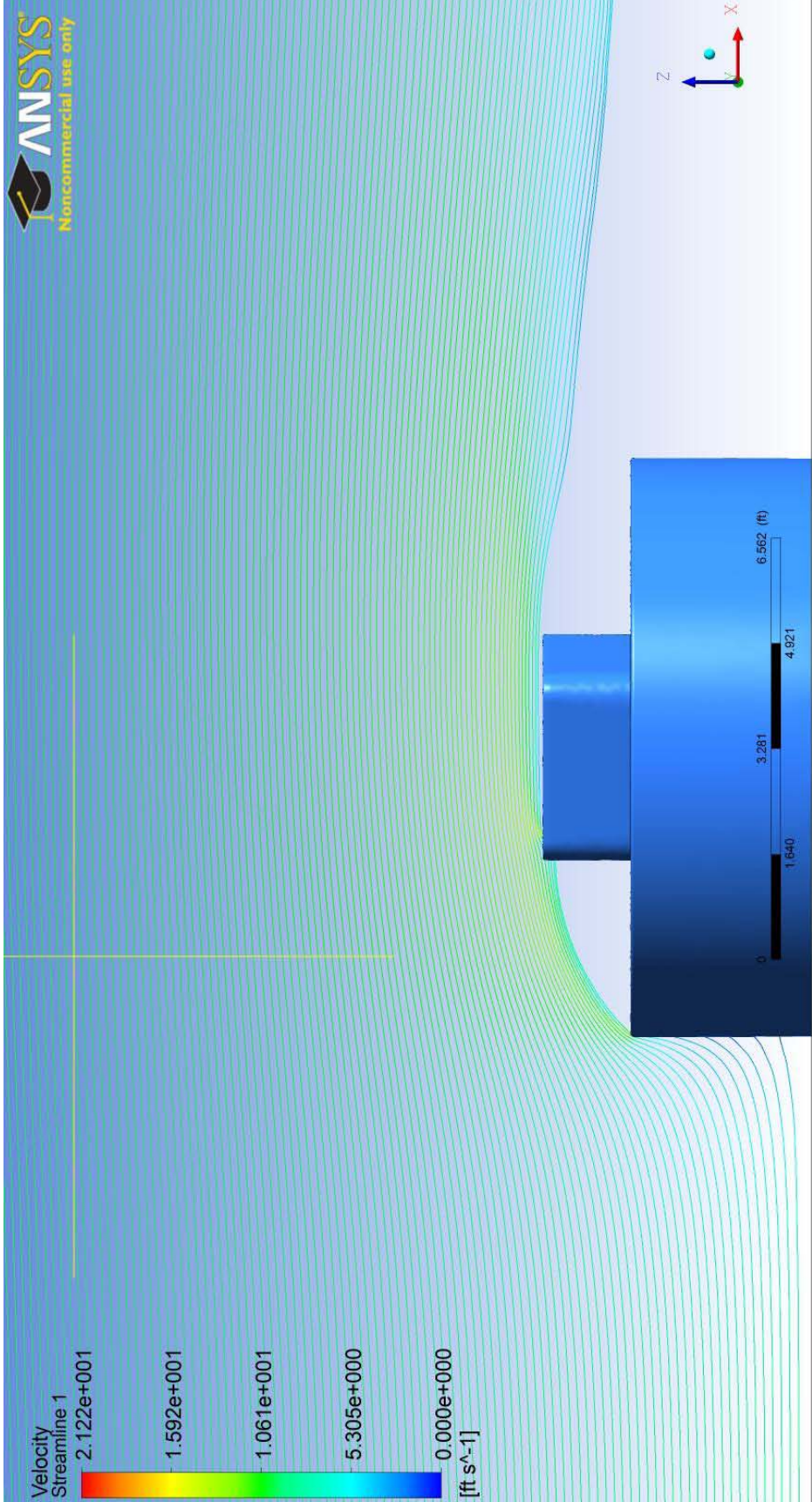
Figure W-3b   WHOI lower model with 30 deg. wind inflow, view 2

41
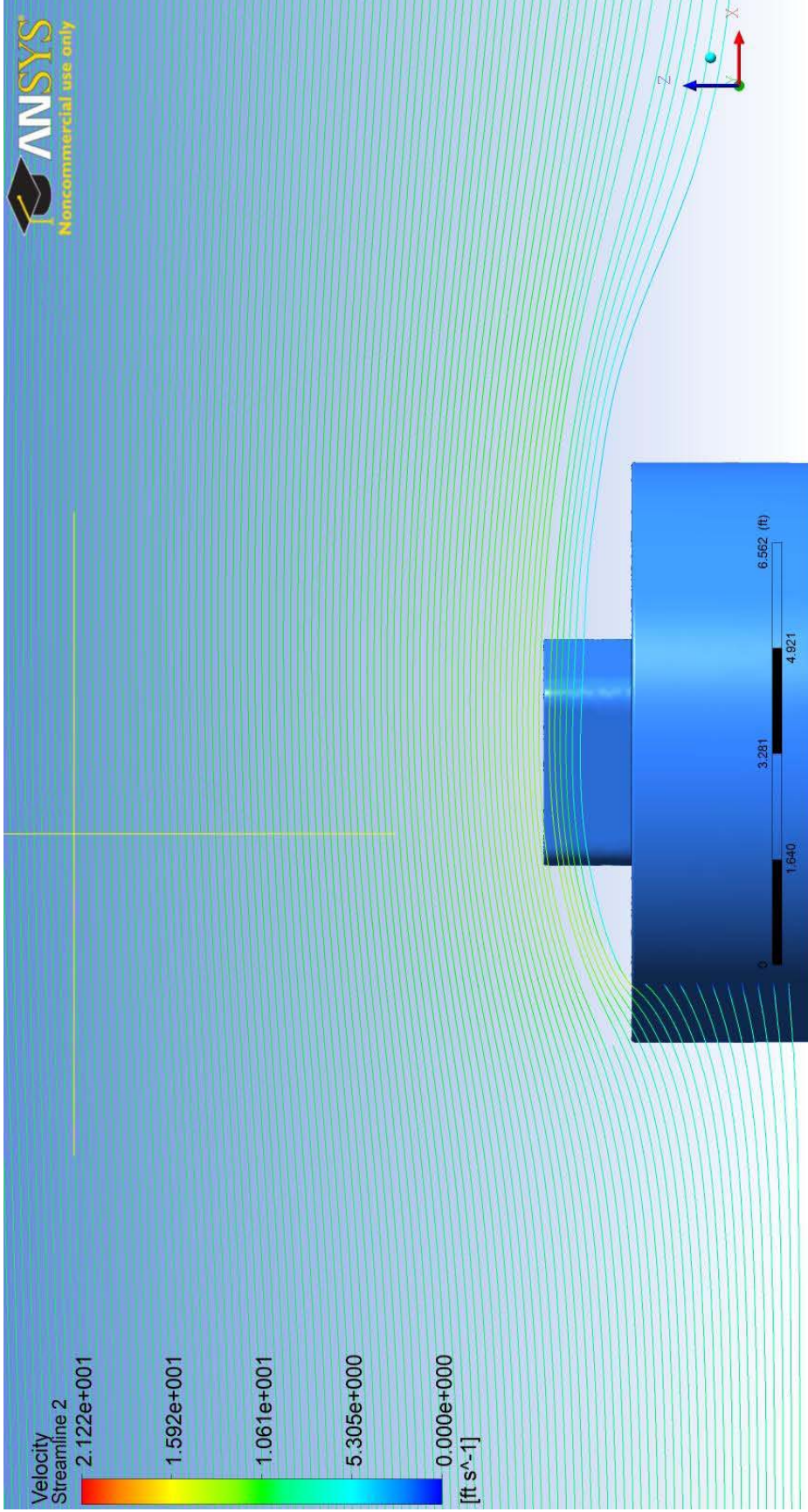
Figure W-3c   WHOI lower model with 30 deg. wind inflow, view 3

42
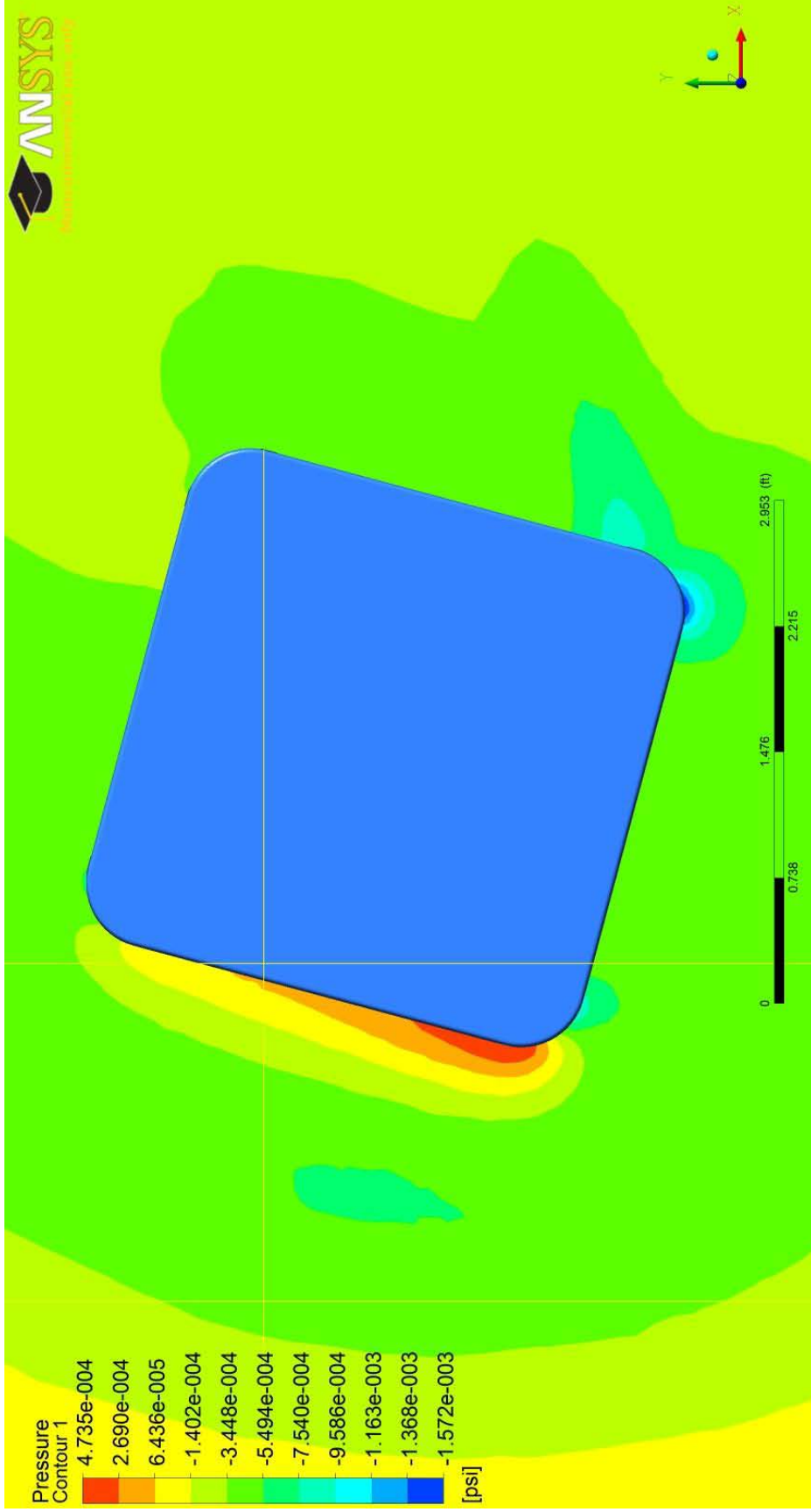
Figure W-3d   WHOI lower model with 30 deg. wind inflow, pressure field

43
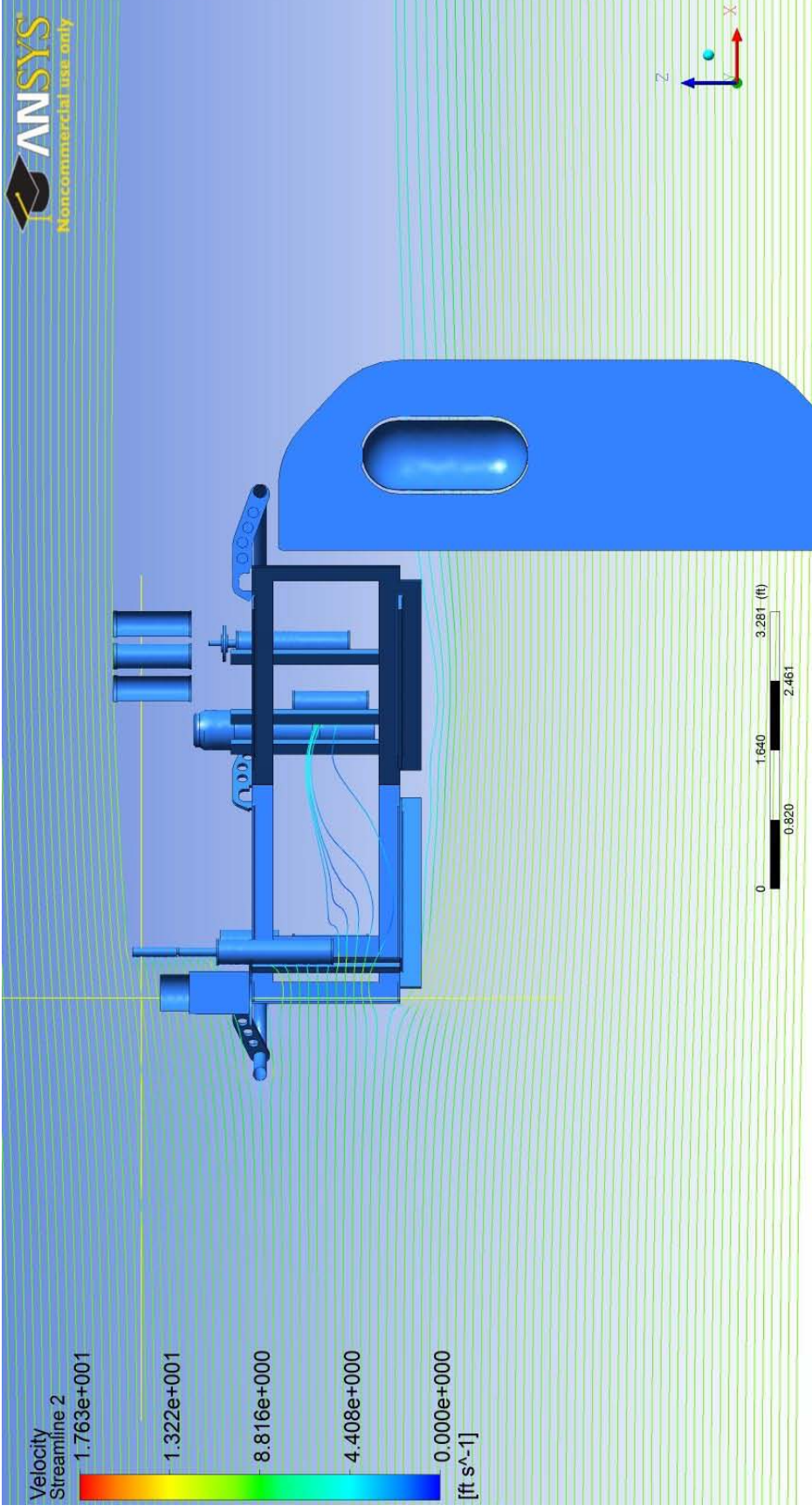
Figure W-4a   WHOI upper half-model with 0 deg. wind inflow, view 1

44
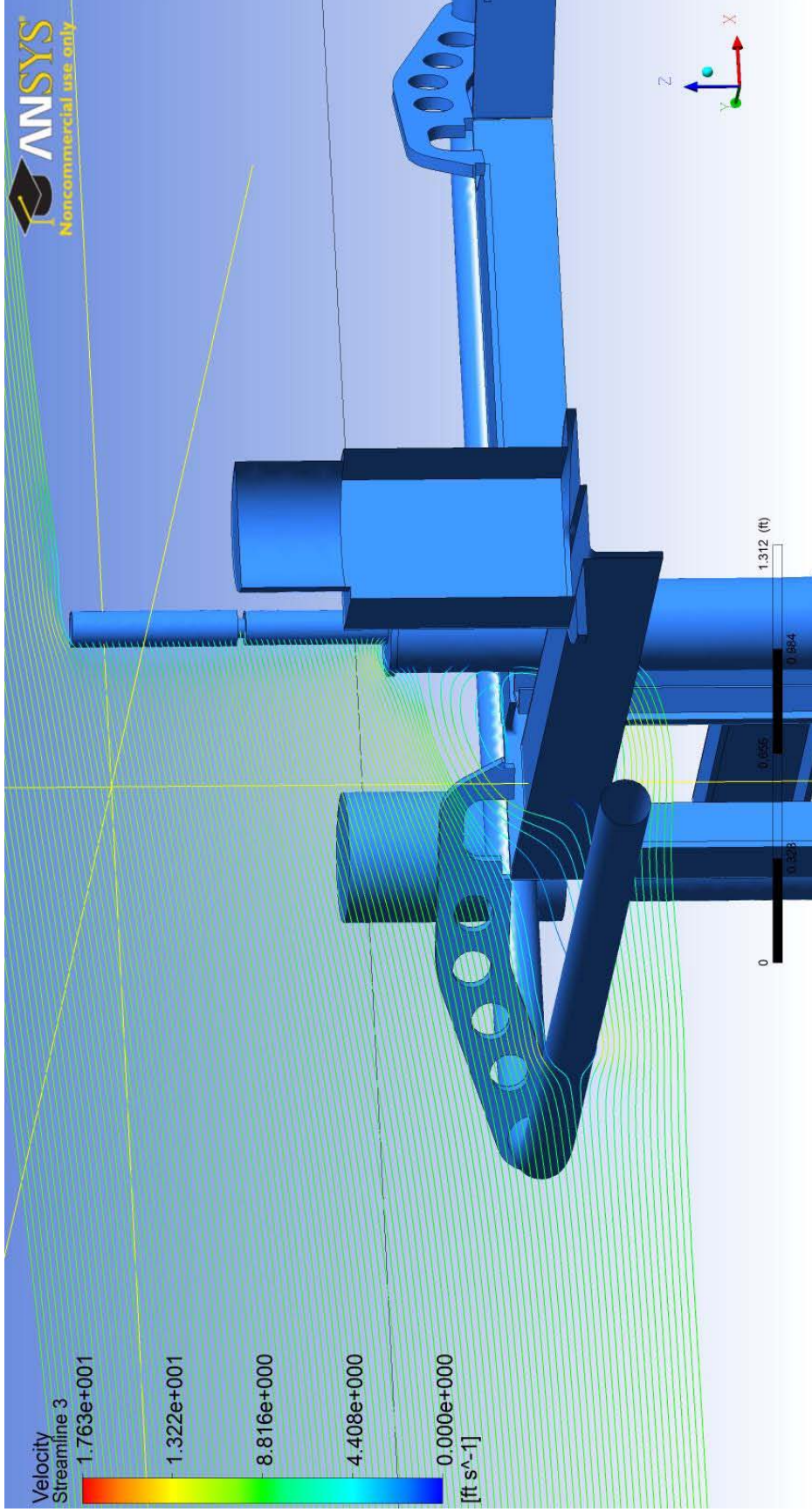
Figure W-4b   WHOI upper half-model with 0 deg. wind inflow, view 2

45

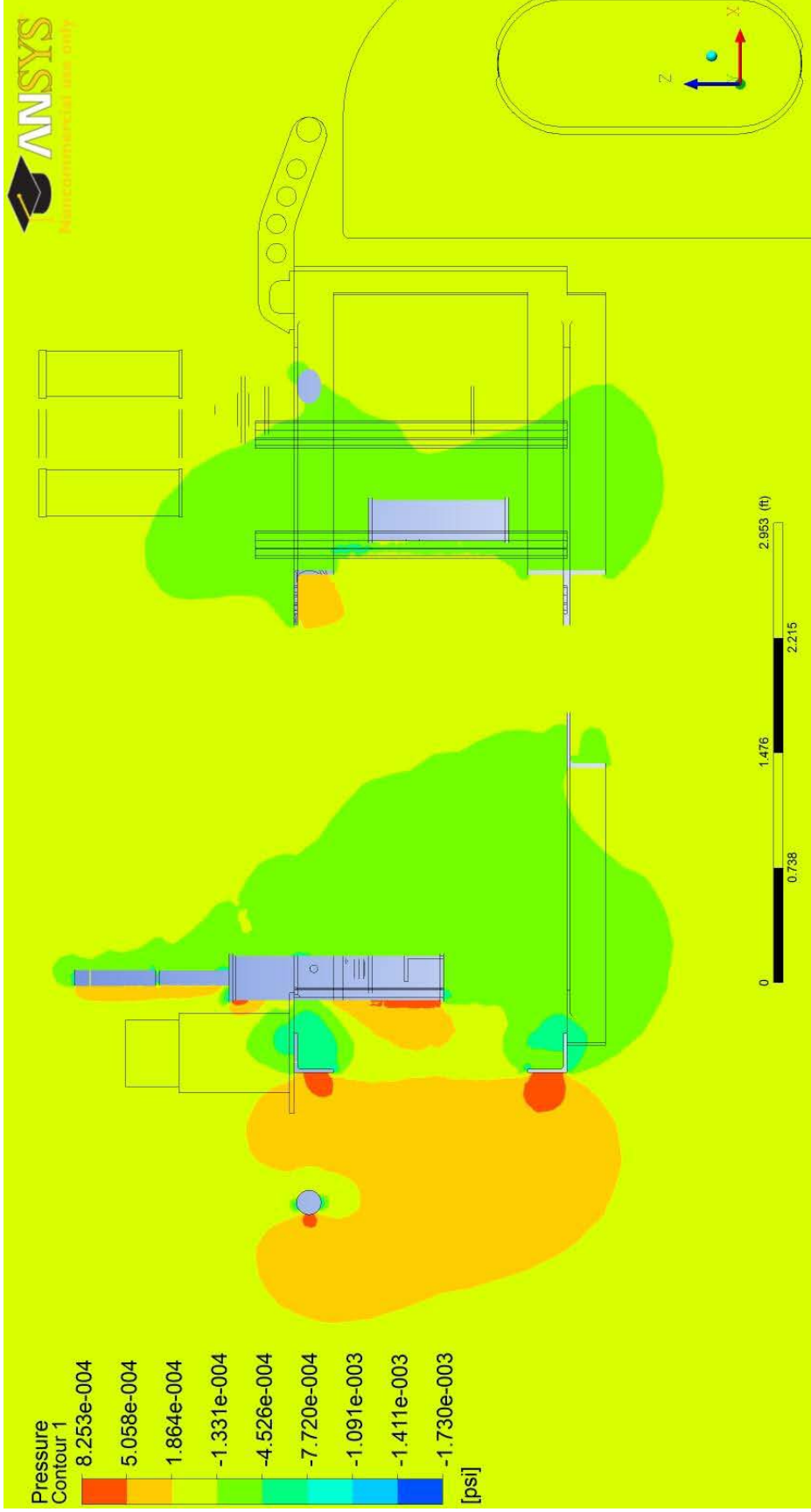Figure W-4c   WHOI upper half-model with 0 deg. wind inflow, view 3

46

Figure W-4d   WHOI upper half-model with 0 deg. wind inflow, view 4

47

Figure W-4e   WHOI upper half-model with 0 deg. wind inflow, view 5

48

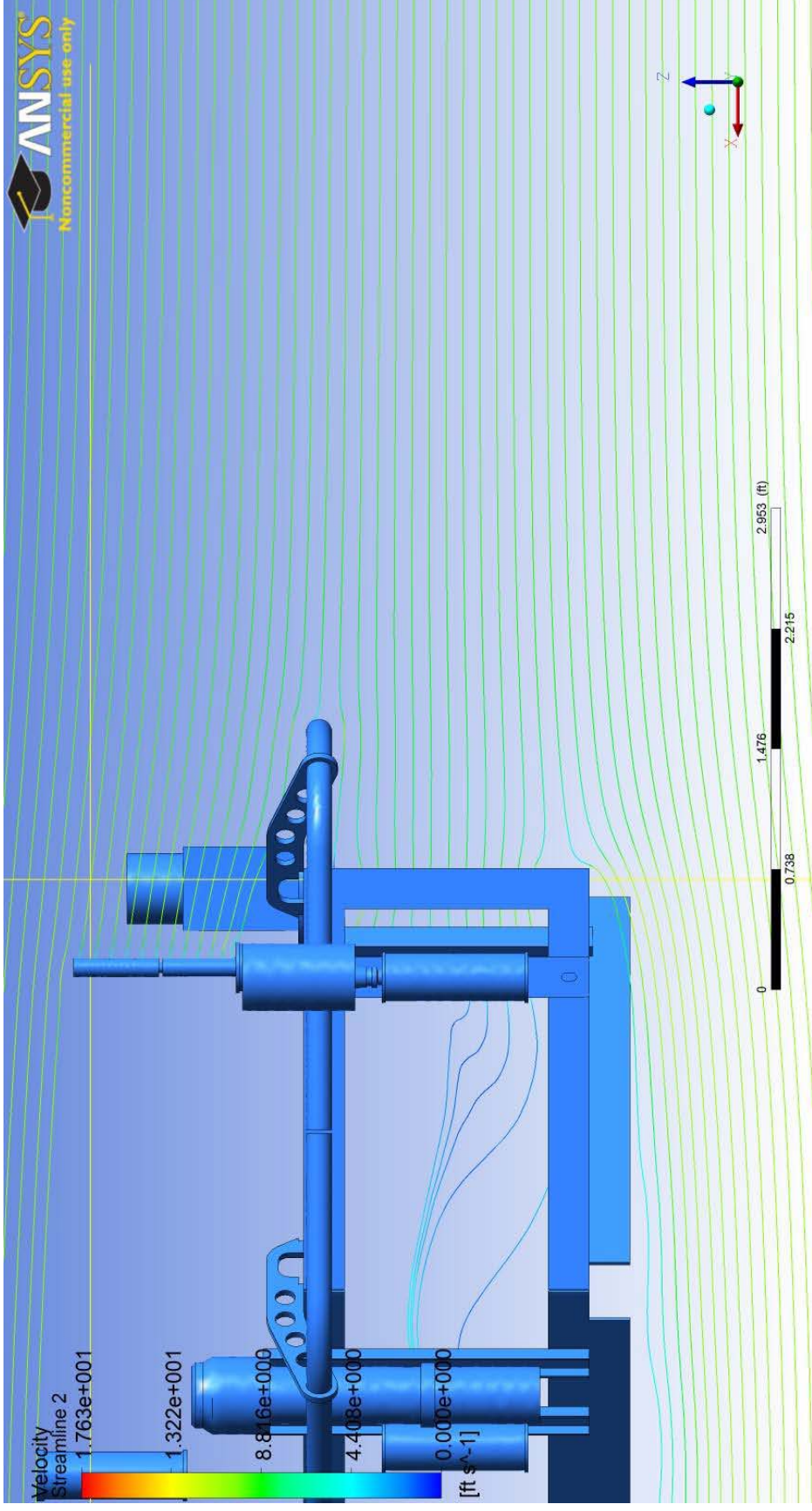Figure W-4f   WHOI upper half-model with 0 deg. wind inflow, pressure field

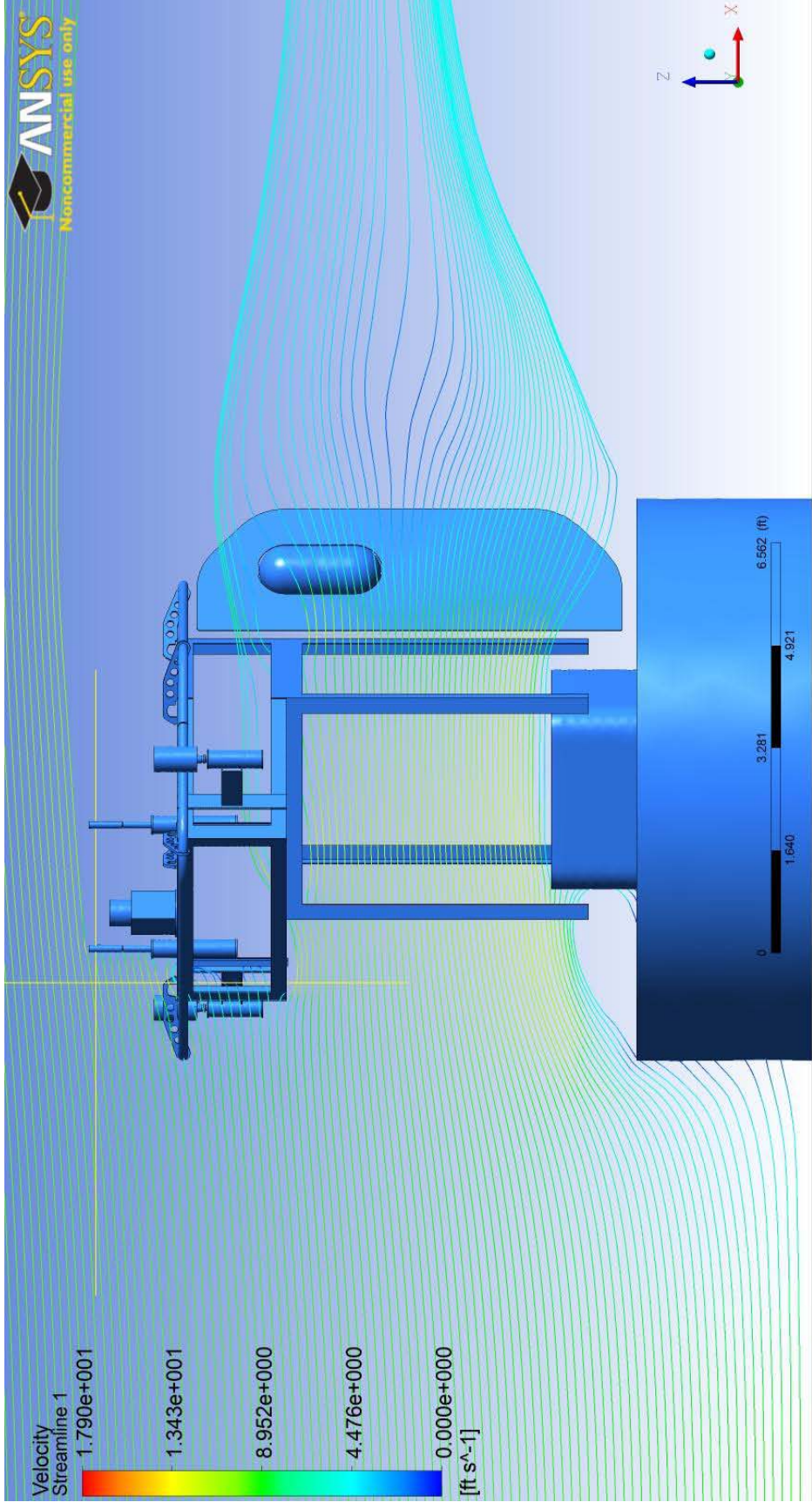Figure W-4g   WHOI upper half-model with 0 deg. wind inflow, view 6

50

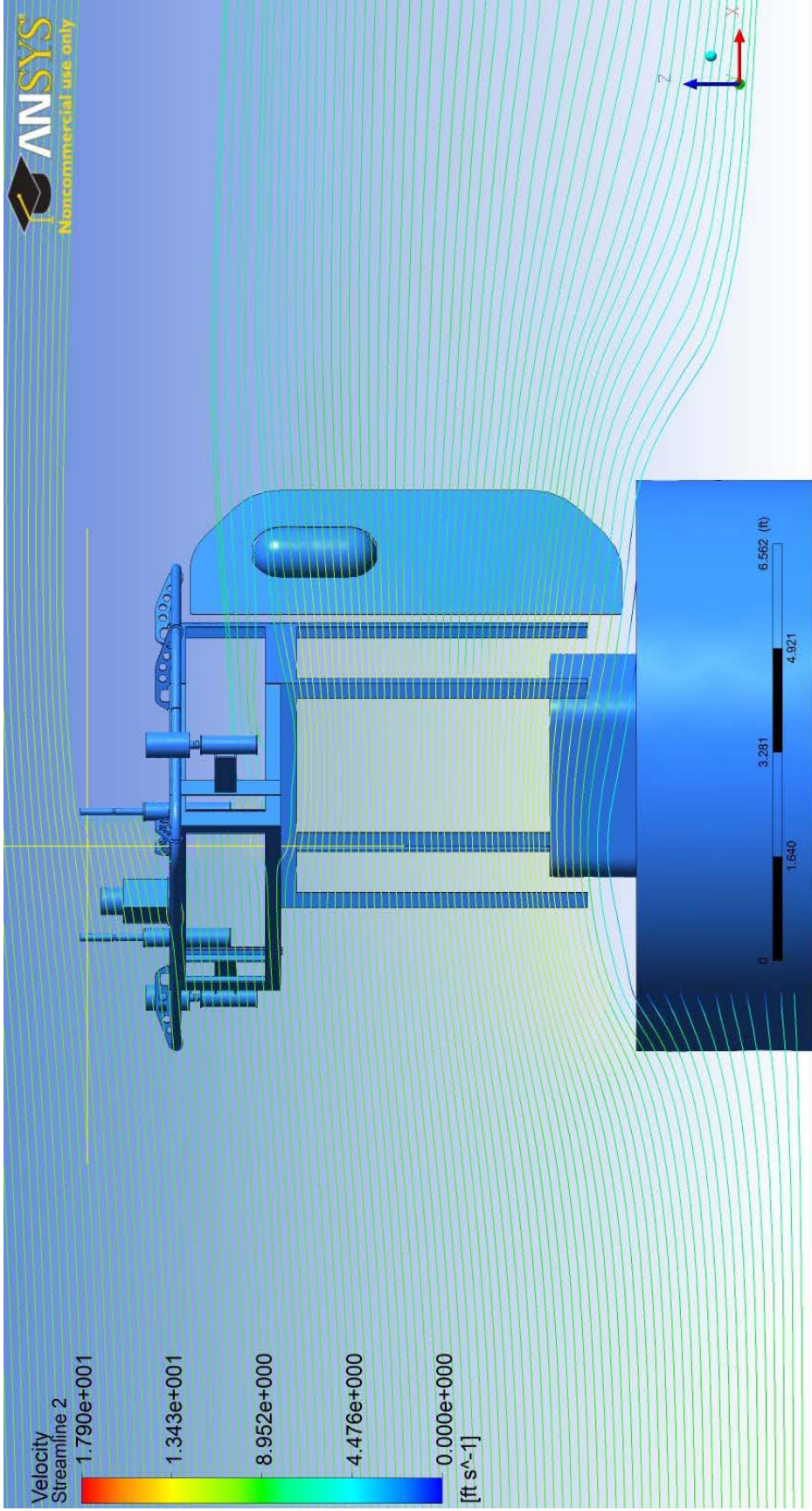Figure W-5a   WHOI full model with 30 deg. wind inflow, view 1

51

Figure W-5b   WHOI full model with 30 deg. wind inflow, view 2
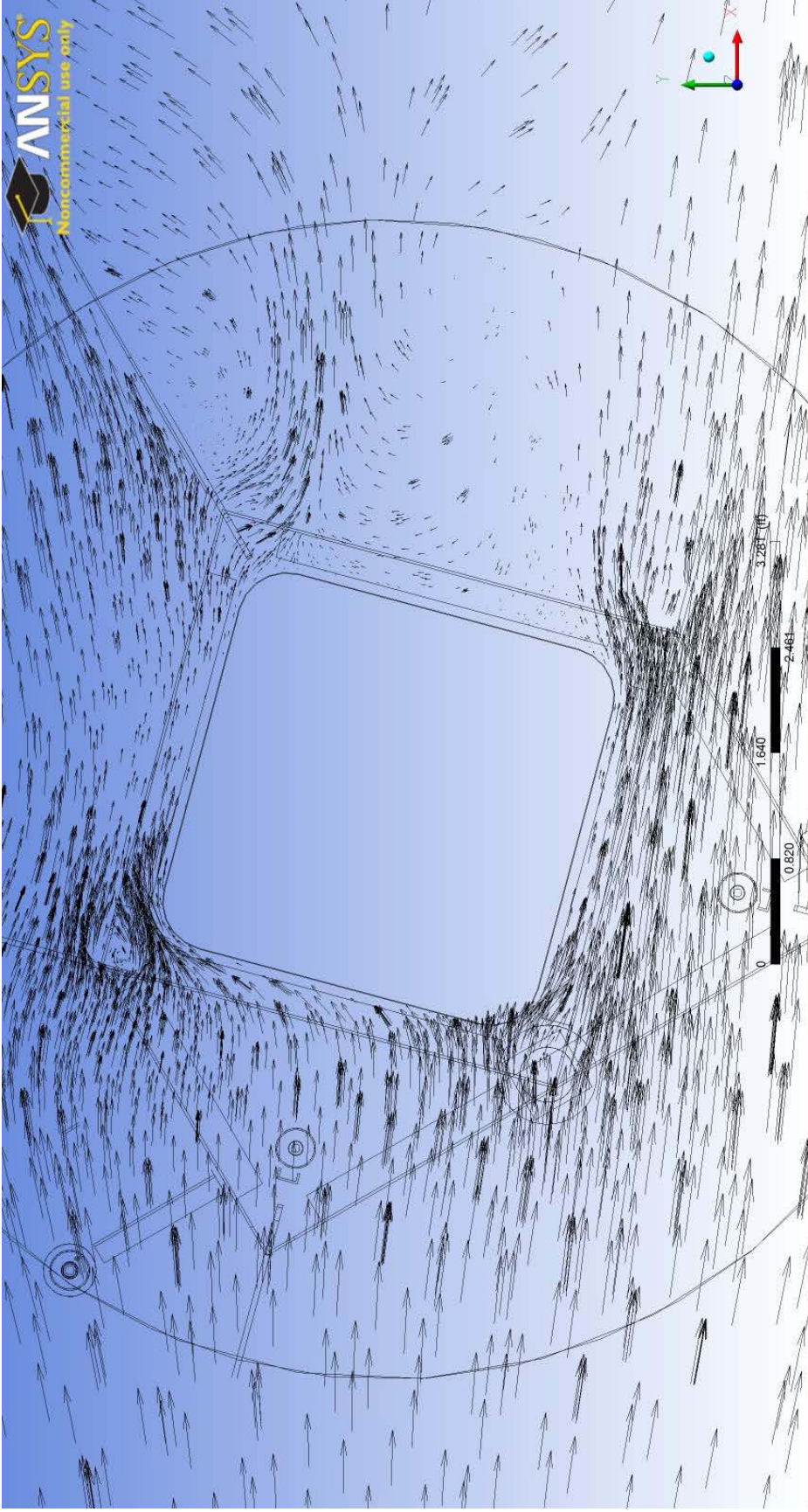
52

Figure W-5c   WHOI full model with 30 deg. wind inflow, view 3
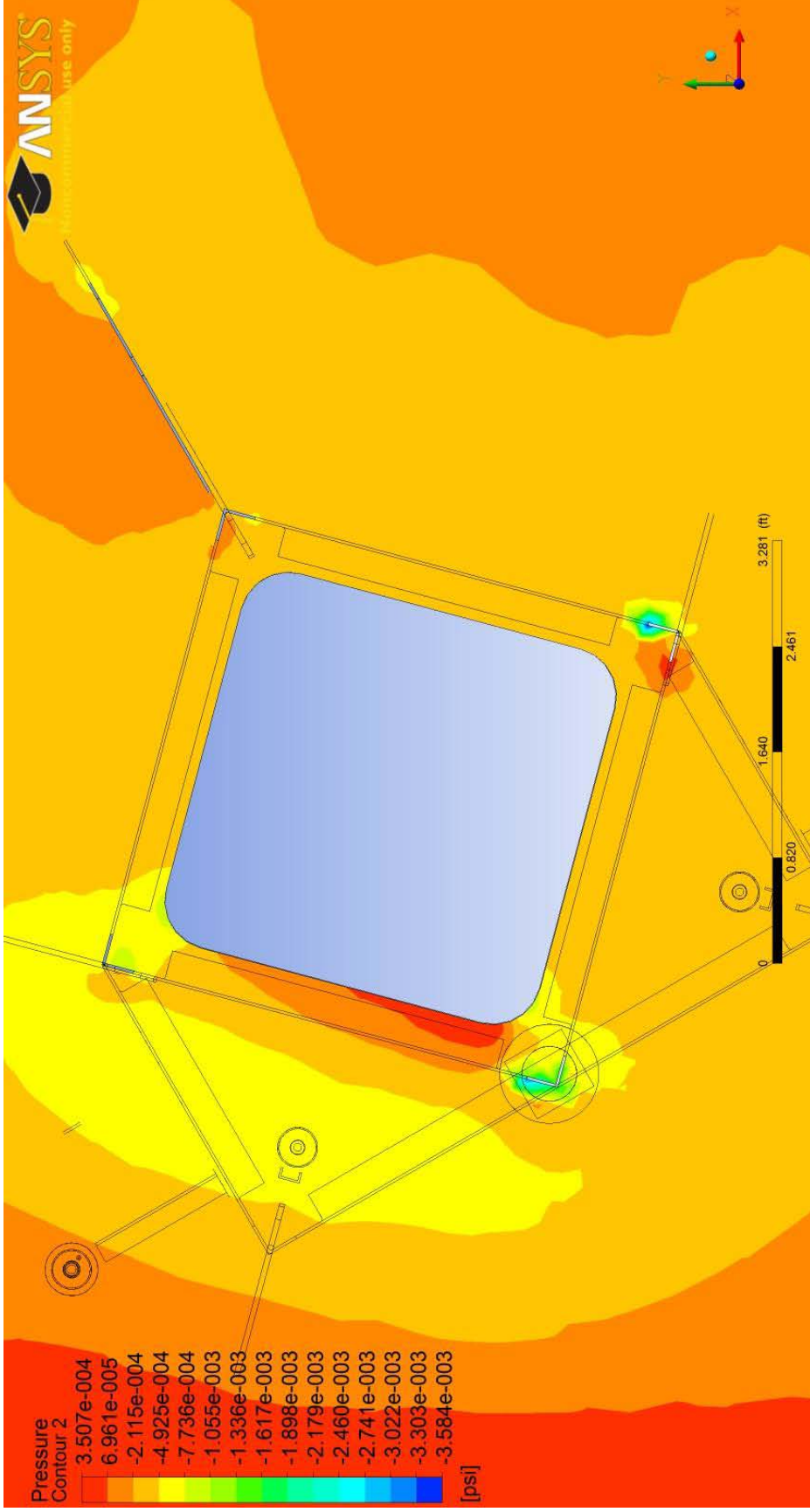
53

Figure W-5d   WHOI full model with 30 deg. wind inflow, pressure field
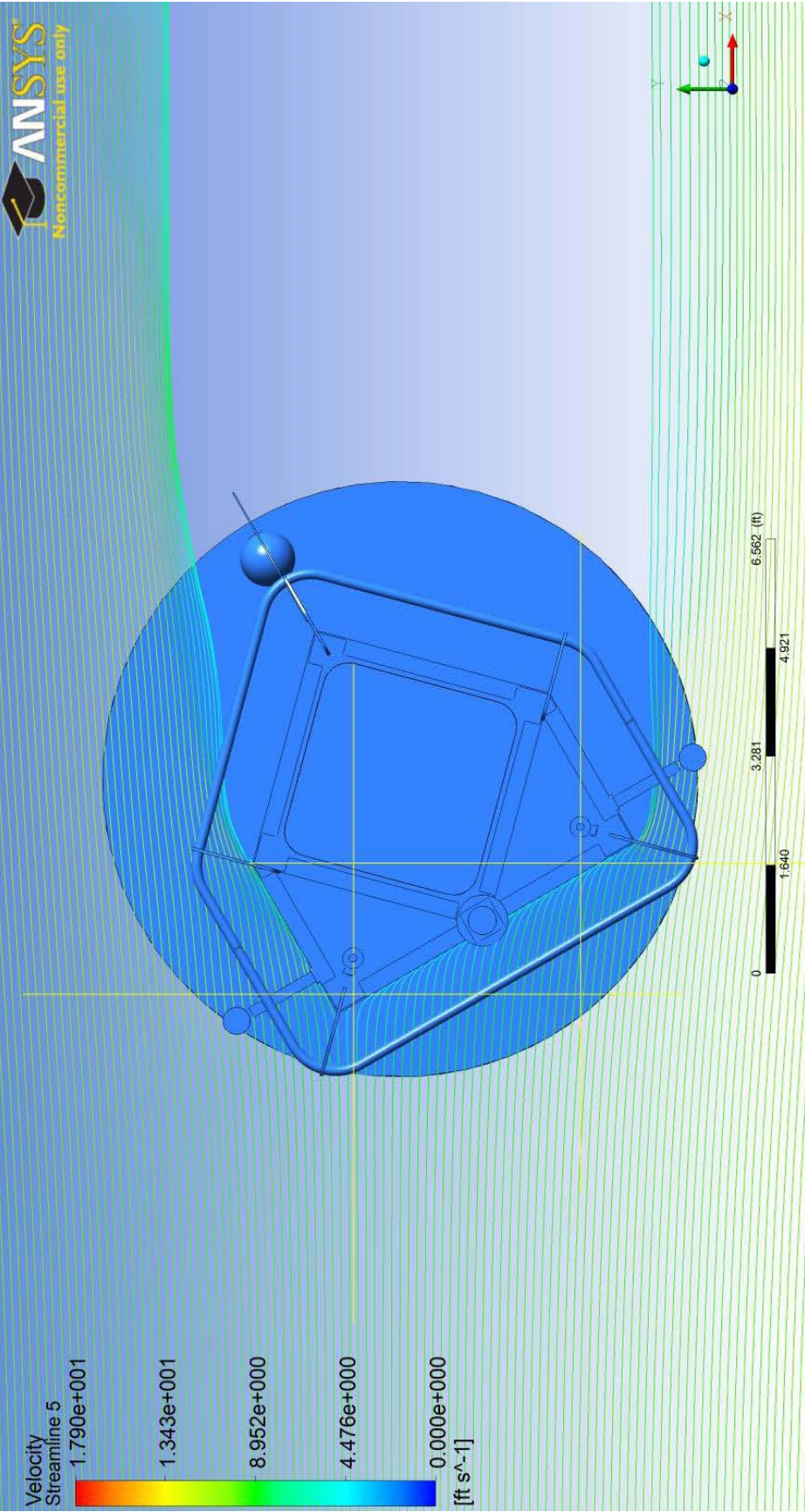
54

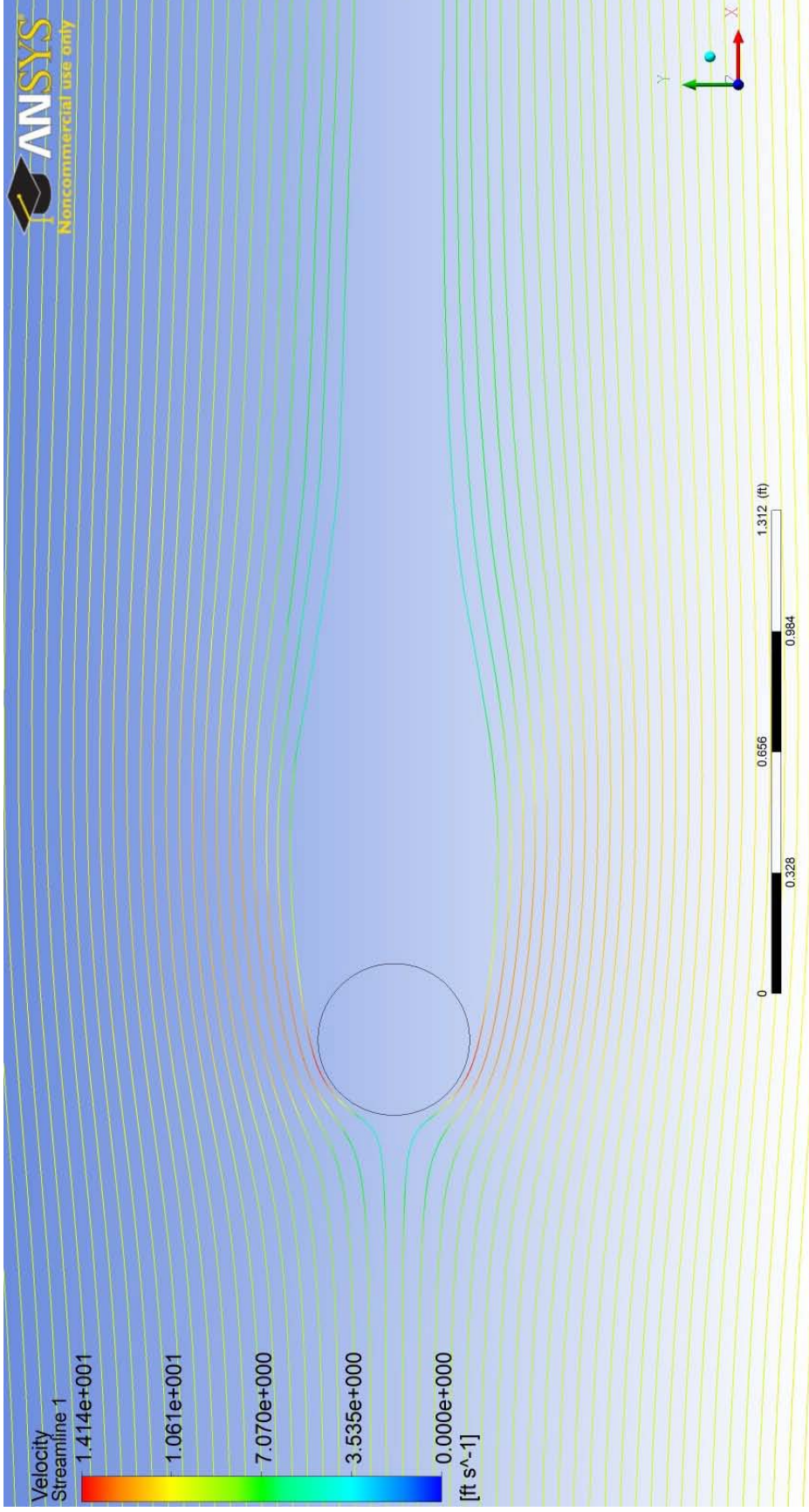Figure W-5e   WHOI full model with 30 deg. wind inflow, top view

55

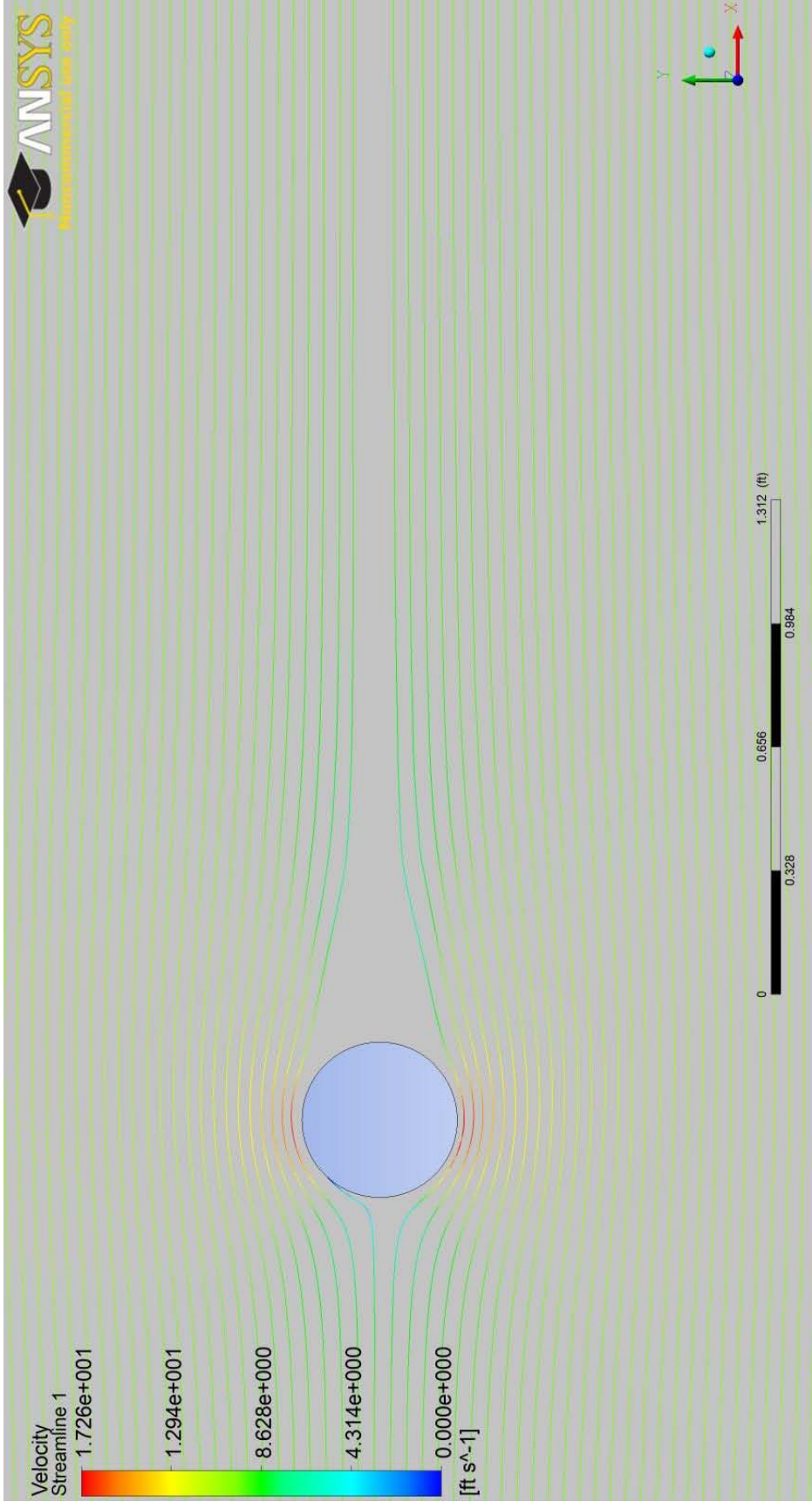Figure V-1   Viscous vs. non-viscous comparison runs: viscous case

56

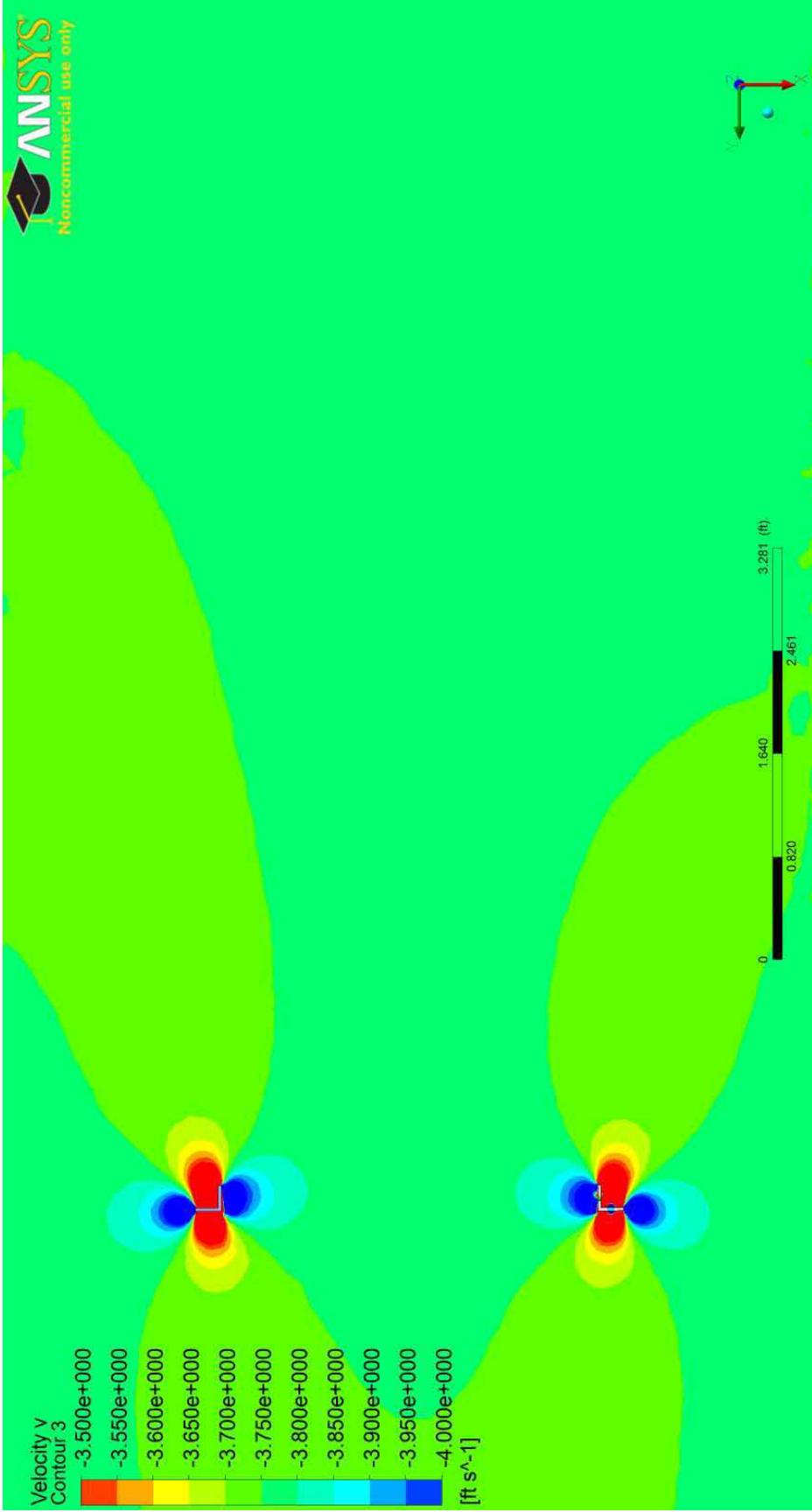Figure V-2 Viscous vs. non-viscous comparison runs: non-viscous case

Figure A-1 Flow disturbance near angle-iron corners

58

50272-101

REPORT DOCUMENTATION PAGE	1. REPORT NO. WHOI-2012-02	2.	3. Recipient's Accession No.

4. Title and Subtitle		5. Report Date
Flow Distortion Investigation of Wind Velocity Perturbations for Two Ocean Meteorological Platforms		March 2012
		6.

7. Author(s) Marc Emond, Doug Vandemark, James Forsythe, Al Plueddemann, Tom Farrar	8. Performing Organization Rept. No.

9. Performing Organization Name and Address	10. Project/Task/Work Unit No.
Woods Hole Oceanographic Institution Woods Hole, Massachusetts 02543	11. Contract(C) or Grant(G) No. (C) (G)

12. Sponsoring Organization Name and Address	13. Type of Report & Period Covered
Woods Hole Oceanographic Institution	Technical Report
	14.

15. Supplementary Notes

This report should be cited as: Woods Hole Oceanographic Institution Tech. Report., WHOI-2012-02.

16. Abstract (Limit: 200 words)

A computational fluid dynamics (CFD) study was performed of the wind flow around two ocean buoys used to collect meteorological data from sensors mounted on the buoy tower. The CFD approach allowed wind velocity perturbations to be evaluated as a step towards quantifying the impacts of flow distortion on buoy wind measurements. The two buoys evaluated were the Wood Hole Oceanographic Institution WHOI Modular Ocean Buoy System and the University of New Hampshire (UNH) 2.1 m discus buoy. Engineering drawings were used to create a computational mesh for each buoy. Suitable solution methods were then developed and tested, CFD simulations were performed, and the results evaluated. Eleven CFD runs were performed, six for the WHOI buoy and five for the UNH buoy. Highlights of analysis for the WHOI buoy were that horizontal flow distortion was relatively small (<1%) for head-on flow, but that the tendency of the buoy to establish an angle of about 30 degrees relative to the flow resulted in acceleration at one anemometer location and deceleration at the other. Highlights of the analysis for the UNH buoy were that flow distortion of about 5% at the wind sensor location could be cut by about a factor of two by either raising the sensor by 2 ft or removing solar panels.

17. Document Analysis   a. Descriptors

Flow distortion investigation

Modular Ocean Buoy System

fluid dynamics

b. Identifiers/Open-Ended Terms

c. COSATI Field/Group

18. Availability Statement	19. Security Class (This Report) UNCLASSIFIED	21. No. of Pages 66
Approved for public release; distribution unlimited.	20. Security Class (This Page)	22. Price

(See ANSI-Z39.18)   *See Instructions on Reverse*   OPTIONAL FORM 272 (4-77)
(Formerly NTIS-35)
Department of Commerce